JOURNAL OF PETROLOGY | VOLUME 44 | NUMBER 10 | PAGES 1727–1757 | 2003 | DOI: 10.1093/petrology/egg056

Synthesis of Staurolite in Melting Experiments of a Natural Metapelite: Consequences for the Phase Relations in Low-Temperature Pelitic Migmatites

ANTONIO GARCÍA-CASCO[1]*, FAOUZIYIA HAISSEN[2], ANTONIO CASTRO[3], HASSAN EL-HMIDI[3], RAFAEL LUÍS TORRES-ROLDÁN[1] AND GUILLERMO MILLÁN[4]

[1]DEPARTAMENTO DE MINERALOGÍA Y PETROLOGÍA, UNIVERSIDAD DE GRANADA, 18002 GRANADA, SPAIN

[2]DÉPARTEMENT DE GÉOLOGIE, UNIVERSITÉ CHOUAIB DOUKKALI, B.P. 20 EL JADIDA, MOROCCO

[3]DEPARTAMENTO DE GEOLOGÍA, UNIVERSIDAD DE HUELVA, 21819 HUELVA, SPAIN

[4]INSTITUTO DE GEOLOGÍA Y PALEONTOLOGÍA, VIA BLANCA Y CARRETERA CENTRAL, HAVANA, CUBA

RECEIVED NOVEMBER 13, 2002; ACCEPTED MARCH 24, 2003

We document experiments on a natural metapelite in the range 650–775°C, 6–14 kbar, 10 wt % of added water, and 700–850°C, 4–10 kbar, no added water. Staurolite systematically formed in the fluid-present melting experiments above 675°C, but formed only sporadically in the fluid-absent melting experiments. The analysis of textures, phase assemblages, and variation of phase composition and Fe–Mg partitioning with P *and* T *suggests that supersolidus staurolite formed at (near-) equilibrium during fluid-present melting reactions. The experimental results are used to work out the phase relations in the system K_2O–Na_2O–FeO–MgO–Al_2O_3–SiO_2–H_2O appropriate for initial melting of metapelites at the upper amphibolite facies. The* P–T *grid developed predicts the existence of a stable* P–T *field for supersolidus staurolite that should be encountered by aluminous Fe-rich metapelites during fluid-present melting at relatively low temperature and intermediate pressures (675–700°C, 6–10 kbar for $X_{H_2O} = 1$, in the KNFMASH system), but not during fluid-absent melting. The implications of these findings for the scarcity of staurolite in migmatites are discussed.*

KEY WORDS: *metapelites; migmatites; partial melting;* P–T *grid; staurolite*

INTRODUCTION

Staurolite-bearing mineral assemblages are characteristic of medium-grade metapelites, but are scarce at higher grade (Pattison & Tracy, 1991). The rare cases in which staurolite appears to be stable at high grade are explained in terms of the enhancement of its stability as a result of the lack of quartz and/or the effect of Zn (e.g. Hollister, 1969; Ashworth, 1975; Goodman, 1993), but most reports of staurolite from quartz-bearing high-grade metapelites indicate that it grew during pre- or post-peak metamorphic conditions [i.e. it appears either as relict grains, commonly armoured within porphyroblasts, that survived from pre-high grade conditions (e.g. Misch, 1968; Yardley, 1976, 1978; Jones & Brown, 1990; Whitney & Irving, 1994; Janák *et al.*, 1999), or as retrograde grains formed during subsequent cooling or a distinct thermal pulse (e.g. Dirks *et al.*, 1991; Graessner & Schenk, 2001; Wilson & Powell, 2001)].

Experimental and theoretical studies (Richardson, 1968; Ganguly, 1972; Rao & Johannes, 1979; Yardley, 1981; Dutrow & Holdaway, 1989; Holdaway *et al.*, 1995) have shown that Fe-St + Qtz is not stable at >700°C, strengthening the idea that the thermal

*Corresponding author. Telephone: +34 958 246613. Fax: +34 958 243368. E-mail: agcasco@ugr.es

stability of staurolite does not reach the solidus temperature of quartz-bearing metapelites of normal composition (Grant, 1973). [Throughout this paper, mineral abbreviations are after Kretz (1983), except: Als, Al-silicate (kyanite, sillimanite or andalusite); Fib, fibrolitic sillimanite; L, silicate melt; V, H_2O-bearing fluid.] However, synthesis of staurolite coexisting with quartz in fluid-absent and fluid-present melting runs of natural schists, metagreywackes and gneisses has been reported sporadically (Vielzeuf & Montel, 1994; Montel & Vielzeuf, 1997; Patiño Douce & Harris, 1998; Castro *et al.*, 1999). The theoretical suggestion by Thompson & Connolly (1995) and Spear *et al.* (1999) that the prograde decomposition of medium-grade staurolite (+ Qtz + Ms) may be verified through fluid-absent melting reactions rather than through subsolidus reactions has profound consequences for the understanding of the behaviour of staurolite at high-grade conditions. An important corollary of the above statement, which emerges from the theory of phase relationships, is that St + Qtz + Ms should be stable above the fluid-present solidus of metapelites (see Spear *et al.*, 1999). In this paper we give the experimental foundation for this corollary, and explore its implications for the phase relations in low-temperature pelitic migmatites.

STARTING MATERIAL

The experiments were performed using a medium-grade metapelite rich in graphite (sample IJ44; Table 1) from the metamorphic terrane of the Isle of Pines, western Cuba, collected close to the village of Nueva Gerona [see Millán (1981, 1997*a*, 1997*b*), Somin & Millán (1981) and García-Casco *et al.* (2001) for geological and petrological information]. The Isle of Pines terrane constitutes a continental platform sequence of Jurassic to Cretaceous terrigenous and carbonate metasediments, with occasional metabasite intercalations, that underwent low- to high-grade metamorphism spanning 350–750°C at pressures of 10–12 kbar during the Late Cretaceous (pre-72 Ma) collision of the terrane with the Cretaceous volcanic arc of Cuba. Collision-related metamorphism was followed by near-isothermal decompression (down to ~3 kbar) at 68 ± 2 Ma, interpreted as the result of tectonic extension (García-Casco *et al.*, 2001). Medium-grade metapelites consist of combinations of garnet, staurolite, kyanite, fibrolite, andalusite, biotite, muscovite, plagioclase and quartz. At high-grade conditions fluid-present partial melting of similar metapelites formed trondhjemitic migmatites that consist of combinations of the same phases except for the lack of staurolite. The leucocratic segregations are trondhjemitic but contain primary muscovite and, locally, accessory K-feldspar. The estimated peak P–T conditions are 700–750°C, 10–12 kbar (García-Casco *et al.*, 2001). Sample IJ44 was selected for experimental investigation of the partial melting processes in the terrane. This sample is composed of Grt–Ky–Fib–Bt–Ms–Pl–Ilm–Qtz, in addition to graphite in significant amounts and accessory apatite, tourmaline, zircon, pyrrhotite, and minor retrograde chlorite after garnet. Garnet forms zoned porphyroblasts, with high-Mn cores and high-Mg rims that record prograde growth, and are systematically replaced by biotite and fibrolite grown upon decompression. The peak metamorphic conditions of this sample are 600–650°C, 10–12 kbar [calculated with the same methods and calibrations as used by García-Casco *et al.* (2001)].

The composition of sample IJ44 approaches that of normal pelites, similar to the North American shale composition, except for somewhat higher MnO and lower MgO and CaO contents (Fig. 1a). This divergence, however, is also characteristic of metapelitic or gneissic materials used in other experimental studies (Fig. 1a). The basic relationships among bulk composition, starting material and run products are shown in the Al_2O_3–K_2O–Na_2O (AKN), an–ab–or, Al_2O_3–$KAlO_2$–FeO (AKF) and Al_2O_3–FeO–MgO (AFM) phase diagrams of Fig. 1b–e. It is apparent that sample IJ44 is saturated in Al_2O_3 relative to the muscovite–plagioclase assemblage, but it is moderately aluminous, as it projects with similar Al_2O_3 content to that of garnet in the AFM diagram. Broadly, sample IJ44 compares well with the metapelitic material used by Patiño Douce & Harris (1998) and Vielzeuf & Holloway (1988) in their experiments (PDH-MBS and VH, respectively, in Fig. 1b–e).

EXPERIMENTAL PROCEDURES

The powder used in the experiments was obtained after milling of ~1000 cm^3 of sample, with further milling of aliquots in an agate mortar. The aliquots were contained in welded gold capsules, of 2·4 mm inner diameter with 0·3 mm wall, and heated at 120°C in an oven for 24 h. We used an end-loaded, solid-medium, piston-cylinder apparatus (University of Huelva) and 12·7 mm (0·5 inch) diameter NaCl–graphite cell assemblies. Oil pressures were measured with electronic DRUCK PTX 1400 pressure transmitters, connected to OMRON E5CK controllers. Temperatures were measured and controlled with Pt100–Pt87Rh13 thermocouples wired to Eurotherm 808 controllers [see Castro *et al.* (1999, 2000) for further details].

Experiments covered the ranges 650–775°C, 6–14 kbar with 10 wt % added H_2O, and 700–850°C, 4–10 kbar with no added H_2O. The experiments lasted 72–339 h (no added H_2O) and 70–192 h (added

Table 1: Composition (average and 1σ) of the starting material

	Bt ($n = 44$)	Ms ($n = 17$)	Grt ($n = 214$)	Ilm ($n = 4$)	Pl ($n = 66$)	Turm ($n = 3$)	Chl ($n = 14$)	Qtz	Ky + Sil	Ap	IJ44
Mode*	18·2	13·2	4·9	0·2	14·1	0·1		40·6	8·3	0·4	
Mode†	20	10–15	5	<1	10–15	<1	<1	41	<10	<1	
SiO_2	35·51 (0·52)	46·60 (0·77)	38·04 (0·49)		62·48 (1·00)	36·94 (0·60)	25·36 (0·40)				62·55
TiO_2	2·90 (0·33)	0·84 (0·32)	0·07 (0·06)	51·11 (0·89)		0·80 (0·20)	0·13 (0·10)				0·99
Al_2O_3	19·84 (0·52)	35·90 (0·68)	20·82 (0·59)	0·38 (0·27)	23·39 (0·65)	32·25 (0·17)	21·39 (0·82)				18·41
FeO_{total}‡	21·37 (0·44)	1·21 (0·16)	33·54 (1·06)	42·96 (1·25)	0·25 (0·18)	5·85 (1·25)	31·86 (2·55)				6·73
MnO	0·20 (0·08)	0·03 (0·05)	2·29 (1·69)	3·60 (1·45)		0·04 (0·04)	0·42 (0·11)				0·15
MgO	6·99 (0·37)	0·55 (0·16)	2·40 (0·32)	0·10 (0·13)		6·34 (1·19)	8·74 (1·64)				1·74
CaO	0·02 (0·03)	0·01 (0·03)	3·68 (0·93)		5·16 (0·46)	0·67 (0·05)					1·19
Na_2O	0·29 (0·13)	0·64 (0·15)			8·10 (0·44)	1·72 (0·15)					1·22
K_2O	9·07 (0·26)	10·03 (0·36)			0·21 (0·06)	0·15 (0·22)					3·37
P_2O_5											0·18
LOI											2·83
Sum	96·20 (0·73)	95·82 (0·76)	100·78 (1·96)	98·14 (0·46)	99·40 (1·15)	84·75 (0·93)	87·90 (1·09)				99·35
Normalization:	22 O	22 O	12 O	6 O & 4 cat	8 O	49 O	28 O			CIPW norm	
Si	5·39 (0·07)	6·15 (0·07)	3·03 (0·03)		2·78 (0·03)	6·08 (0·07)	5·52 (0·12)			Qtz	34·04
Ti	0·33 (0·04)	0·08 (0·03)	0·00 (0·00)	1·97 (0·03)		0·10 (0·02)	0·02 (0·02)			Or	20·65
Al	3·55 (0·08)	5·58 (0·10)	1·96 (0·03)	0·02 (0·02)	1·23 (0·03)	6·25 (0·01)	5·48 (0·15)			Ab	10·68
Fe^{3+}				0·04 (0·05)	0·01 (0·01)					An	5·02
Fe^{2+}	2·71 (0·06)	0·13 (0·02)	2·24 (0·06)	1·81 (0·10)		0·80 (0·17)	5·80 (0·52)			Crn	11·36
Mn	0·03 (0·01)	0·00 (0·01)	0·15 (0·11)	0·16 (0·06)		0·01 (0·01)	0·08 (0·02)			En	4·51
Mg	1·58 (0·08)	0·11 (0·03)	0·28 (0·04)	0·01 (0·01)		1·56 (0·30)	2·83 (0·50)			Fs	11·38
Ca	0·00 (0·01)	0·00 (0·00)	0·32 (0·08)		0·25 (0·02)	0·12 (0·01)				Ilm	1·95
Na	0·09 (0·04)	0·16 (0·04)			0·70 (0·04)	0·55 (0·05)				Ap	0·41
K	1·76 (0·05)	1·69 (0·06)			0·01 (0·00)	0·03 (0·05)					
Mg#	0·37 (0·01)	0·44 (0·09)	0·11 (0·01)	0·00 (0·01)		0·66 (0·09)	0·33 (0·06)				0·35

*Calculated by mass balance after recasting whole-rock and mineral composition in terms of 100 oxi-equivalent units to approach the volume of the phases (using software *CSpace*, Torres-Roldan *et al.*, 2000).
†Calculated by analysis of back-scattered electron images of aliquots of powder (using *NIH* software, Rasband, 1997).
‡Fe_2O_3 for plagioclase.
Mg# = $Mg/(Mg + Fe^{2+})$.

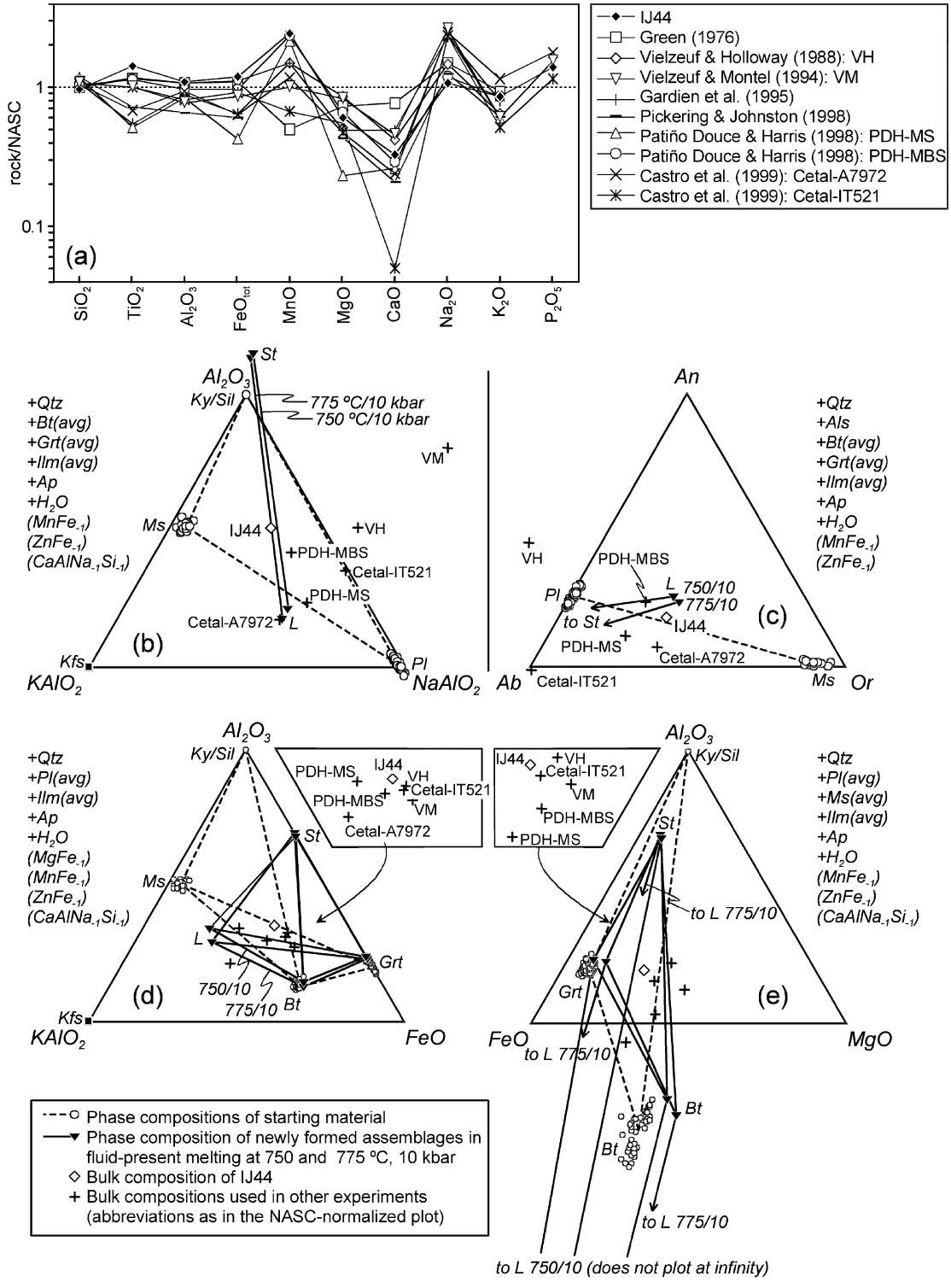

Fig. 1. Characterization of starting material. (a) Bulk composition of sample IJ44 and selected metapelitic or gneissic materials used in other experiments normalized to the North American shale composition (NASC, Gromet *et al.*, 1984). (b)–(e) Projected compositions of sample IJ44 (diamond), phases of the starting material (○), run products of fluid-present melting at 750 and 775°C, 10 kbar (▼), and selected metapelitic or gneissic materials used in other experiments (+; see the NASC-normalized plot for abbreviations) into condensed triangular phase diagrams constructed after projections from combinations of phases from the starting material (Table 1) and exchange vectors, as indicated adjacent to the diagrams. Tie-lines join averages of coexisting phases and arrowed tie-lines point to phases that project at infinity (mapping and diagrams generated using program *CSpace*, Torres-Roldán *et al.*, 2000).

H_2O), with the longest runs corresponding to the experimental conditions close to the solidi. The shorter duration of the fluid-present experiments was intended to avoid H_2O loss from the capsules. However, H_2O loss from gold capsules is not likely to be a serious problem at the temperature of our experiments (Patiño Douce & Beard, 1994; Truckenbrodt & Johannes, 1999). The presence and abundance of graphite in the starting material may have allowed the internal buffering of f_{O_2} in the runs. However, the probable diffusion of hydrogen out of the gold capsules during the experiments hampers a precise estimation of f_{O_2}. Probably, the graphite-based cell assemblies used limit f_{O_2} to values between the quartz–fayalite–magnetite (QFM) buffer and QFM − 2 (Patiño Douce & Beard, 1995). Experimental conditions, duration and mineral assemblages are shown in Table 2 and Fig. 2. Textural details and composition of the run products are presented in Fig. 3 and Tables 3–7, respectively. This study is centred on fluid-present conditions. The fluid-absent experimental results are described, essentially, for comparative purposes.

The addition of 10 wt % H_2O in the fluid-present experiments was intended to ensure excess H_2O in the runs, even at the highest pressure investigated (14 kbar, 700°C) at which the solubility of H_2O in the melt is highest (see Paillat *et al.*, 1992; Holtz *et al.*, 1995, 2001). This is confirmed by the presence of rounded bubbles in the pools of quenched glasses at 14 kbar (Fig. 3a). Assuming no loss of hydrogen, the fluid would be a H_2O–CO_2–CH_4 mixture, with $X_{H_2O} = 0{\cdot}8$–$0{\cdot}9$ (X_{H_2O} increasing with pressure) and equimolar amounts of CO_2 and CH_4, formed after reaction of added H_2O with graphite from the starting material (see French, 1966; Ohmoto & Kerrick, 1977; Connolly & Cesare, 1993). At 14 kbar, 700°C, this fluid composition translates into a solubility of H_2O in the melt of ∼14 wt % [calculated after the Burnham (1994) model] that is not enough to consume the total amount of added water for melt fractions of up to ∼50 wt %. The same conclusion is reached for the whole range of P–T investigated. Upon hydrogen diffusion out of the gold capsules (and, consequently, upon oxidation), the fluid should have lower CH_4 and H_2O and higher CO_2 contents. At a given P–T, lower $X^{fluid}_{H_2O}$ translates into lower H_2O dissolved in the melt (Burnham, 1994), ensuring the presence of an H_2O-rich fluid in all runs with added H_2O. Consequently, the melts formed have maximum H_2O contents for given P–T–$X^{fluid}_{H_2O}$ ($X^{fluid}_{H_2O} \leq 0{\cdot}8$–$0{\cdot}9$).

ANALYTICAL TECHNIQUES

The composition of sample IJ44 was determined by XRF using a Philips PV1404 spectrometer (University of Granada) after fusion with lithium tetraborate. Typical precision was better than ±1·5% (relative) for a concentration of 10 wt %. Phase composition of the starting material was determined at the University of Granada with a CAMECA SX-50 operated at 20 kV and 20 nA and synthetic SiO_2, Al_2O_3, $MnTiO_3$, Fe_2O_3 and MgO, and natural diopside, albite and sanidine as calibration standards, and a ZEISS DSM 950 scanning microscope equipped with a LINK-ISIS energy-dispersive spectrometer operated at 20 kV and 1–2 nA beam current, with counting times of 50–100 s, and the same calibration standards. Phase composition of the run products was determined with a JEOL-JSM5410 scanning microscope (University of Huelva) equipped with a LINK-ISIS energy-dispersive spectrometer operated under similar conditions and using wollastonite, jadeite, orthoclase, corundum, periclase, and metallic Fe and Ti as calibration standards. To minimize the loss of elements during the analysis, the glass (quenched melt) was analysed rastering the 1 μm beam over an area of ∼6 μm^2 (it was not generally possible to analyse larger areas because the pools of melt contain fine-grained solid material; Fig. 3), except in experiments with low melt fractions near the fluid-present and fluid-absent solidi, where it was necessary to use a fixed beam of 1 μm diameter. Experiments to detect the effect of duration of electron bombardment on measured X-ray intensities revealed loss of Na in the glasses, more prominent in those formed in the fluid-present runs. Accordingly, Na contents were measured first, during a third of the total counting time for other elements, and the nominal Na_2O contents were increased by 10–20 wt % (relative) based on two-order polynomial regression models developed for wt % decrease vs time of irradiation.

EXPERIMENTAL RESULTS

Fluid-present experiments

The fluid-present solidus is located at 650–675°C in the range 6–10 kbar and has a steep dP/dT slope (Fig. 2). Similar conditions were calculated by White *et al.* (2001) for the fluid-present solidus of a model Kfs-absent metapelite within the KNCFMASH system. Steep positive slopes were determined experimentally by Storre & Karotke (1972) and Huang & Wyllie (1974) for a similar Kfs-absent reaction involving melting of Ms + Qtz + H_2O in the KASH system at 7–30 kbar. Thermodynamic calculations by Spear *et al.* (1999), Holland & Powell (2001) and White *et al.* (2001) also suggest steep positive slope at 4–14 kbar in the KNASH, KFMASH and KNFMASH systems. In the KNCFMASH system White *et al.* (2001) calculated steep positive slope for reactions that do not involve

Table 2: Experimental conditions and assemblages

Ref.	T (°C)	P (kbar)	t (h)	wt % H_2O	Newly formed phases*	Relict phases/observations
Fluid-present subsolidus experiments						
FH17a	650	10	90	10		Grt–Als–Bt–Qtz–Ms–Pl
AGC1a	650	6	90	10		Grt–Als–Bt–Qtz–Ms–Pl
Fluid-present supersolidus experiments						
FH18a	675	6	70	10	L	Grt–Als–Bt–Qtz–Ms–Pl/very small amount of melt
FH16a	675	10	101	10	L	Grt–Als–Bt–Qtz–Ms–Pl/very small amount of melt
FH19a	700	6	87	10	L–St–Grt–Bt	Grt–Als–Bt–Qtz–Ms/gas bubbles in the melt
FH11a	700	10	120	10	L–St–Grt–Bt	Grt–Als–Bt–Qtz–Ms
FH20a	700	12	96	10	L–St–Grt–Bt	Grt–Als–Bt–Qtz–Ms/small amount of newly formed Bt
FH24a	700	14	97	10	L–St–Grt–Bt	Grt–Als–Bt–Qtz–Ms/gas bubbles in the melt; small amount of newly formed Bt
FH22a	725	8	96	10	L–St–Grt–Bt	Grt–Als–Bt–Qtz
FH10a	725	10	144	10	L–St–Grt–Bt	Grt–Als–Bt–Qtz–Ms
FH23a	725	12	96	10	L–St–Grt–Bt	Grt–Als–Bt–Qtz
FH09′a	750	10	134	10	L–St–Grt–Bt	Grt–Als–Bt–Qtz/very small amount of Qtz
FH08′a	775	10	134	10	L–St–Grt–Bt	Grt–Als–Bt–Qtz/very small amount of Qtz
Fluid-absent subsolidus experiments						
FH14a	700	4	264	0		Grt–Als–Bt–Qtz–Ms–Pl
AGC2a	750	10	264	0		Grt–Als–Bt–Qtz–Ms–Pl
Fluid-absent supersolidus experiments						
FH15a	725	4	263	0	L–Kfs–Bt–St	Grt–Als–Bt–Qtz–Ms–Pl
FH06a	725	6	339	0	L	Grt–Als–Bt–Qtz–Ms–Pl/small amount of melt (within the interior of Pl and Ms)
FH02a	750	6	72	0	L–Kfs–Bt–Als–Pl	Grt–Als–Bt–Qtz–Ms–Pl
FH03b	750	6	264	0	L–Kfs–Bt–Als–Pl	Grt–Als–Bt–Qtz–Ms–Pl
FH08a	775	6	115	0	L–Kfs–Bt–Pl	Grt–Als–Bt–Qtz–Ms–Pl
FH07a	775	10	263	0	L–Kfs–Bt–Grt–Pl	Grt–Als–Bt–Qtz–Ms–Pl/zoned Pl
FH09a	800	6	90	0	L–Kfs–Bt–Als–Pl	Grt–Als–Bt–Qtz–Ms–Pl/melt within the interior of Pl
FH12a	800	10	166	0	L–Bt–Grt–Pl	Grt–Als–Bt–Qtz–Ms–Pl
FH05a	825	6	137	0	L–Bt–Grt–Als–Pl–St–Spl	Grt–Als–Bt–Qtz–Ms–Pl/Ms, Qtz and Pl nearly exhausted
FH13a	825	10	166	0	L–Kfs–Bt–Grt	Grt–Als–Bt–Qtz–Ms–Pl/minute amounts of relict Ms and Bt
FH04a	850	6	238	0	L–Kfs–Bt–Grt–Als–Spl	Grt–Als–Bt–Qtz–Pl/zoned Pl; Bt reacting out

*Includes newly formed compositions of garnet, biotite and plagioclase.

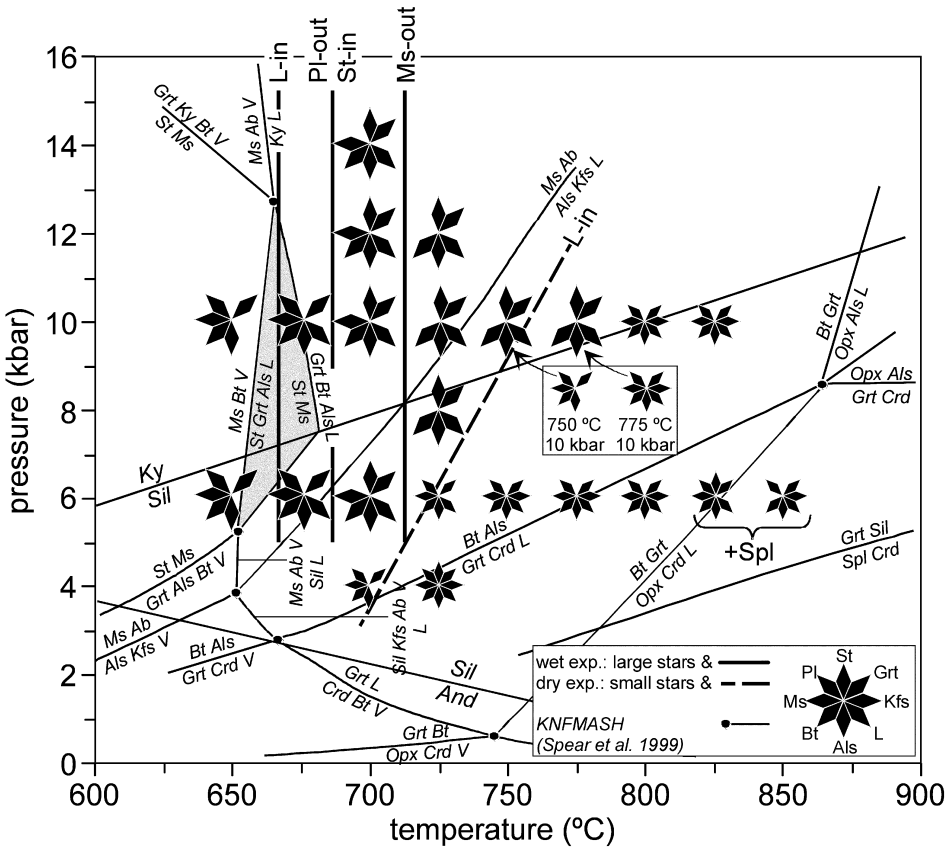

Fig. 2. *P–T* projection of the fluid-present (large stars) and fluid-absent (small stars) experimental runs with indications of the assemblages present, lines for the appearance or disappearance of phases, and the KNFMASH grid of Spear *et al.* (1999). The shaded area in this grid shows the predicted field of St + L stability.

garnet (at 4–6 kbar) and steep negative slope for reactions producing garnet (at 6–12 kbar). Given the experimental uncertainty of our brackets, the fluid-present solidus of sample IJ44 is drawn vertical (Fig. 2, L-in). It should be noted that this solidus does not compare with the fluid-present solidus of Kfs-bearing granitic or gneissic rocks, which has a negative dP/dT slope.

The amount of melt produced at 675°C is very small and located in isolated pools of <5–10 μm in size, and it increases significantly at 700°C. At $\geq$700°C, idiomorphic staurolite formed (Fig. 3a–e). The melting process is accompanied by a decrease in the contents of plagioclase, muscovite, quartz, fibrolite and kyanite. All of the reactant phases dissolved into the melt, except kyanite, which is isolated from the molten matrix by staurolite mantles around it (Fig. 3a–e). This corona-like texture indicates a reaction relationship between kyanite and staurolite. The decrease in plagioclase is significant, and it is exhausted at $\geq$700°C, arguing for an important contribution of this phase to the melting process. Following plagioclase, muscovite is exhausted at $\geq$725°C. Quartz was not exhausted, but it is barely present at 750 and 775°C as very small grains dispersed within the melt or aggregated with Al-silicate. Kyanite and sillimanite were not exhausted, appearing as relict grains or aggregates of grains replaced by melt. Adjacent to the solidus (675°C isotherm) relict garnet and biotite apparently did not participate in the melting reactions, but they appear to be dissolved at higher temperature. However, new compositions formed at the dissolving rims of garnet (inset in Fig. 3a; see also Fig. 6a, below) and in idiomorphic crystals of biotite grown within the melt (Fig. 3c–e; see also Fig. 6c, below).

The reactions implied in the fluid-present experiments have been evaluated following the approach of Fisher (1989) using *CSpace* software (Torres-Roldán *et al.*, 2000). All the models include the composition of the run products (melt, staurolite and the newly formed compositions of garnet and biotite) and the phases from the starting material (quartz, muscovite, plagioclase, Al-silicate, ilmenite, garnet and biotite) in the eight-component system SiO_2, TiO_2, Al_2O_3, FeO, MgO, CaO, Na_2O and K_2O. Minor components MnO and ZnO, and H_2O (and, consequently, phase

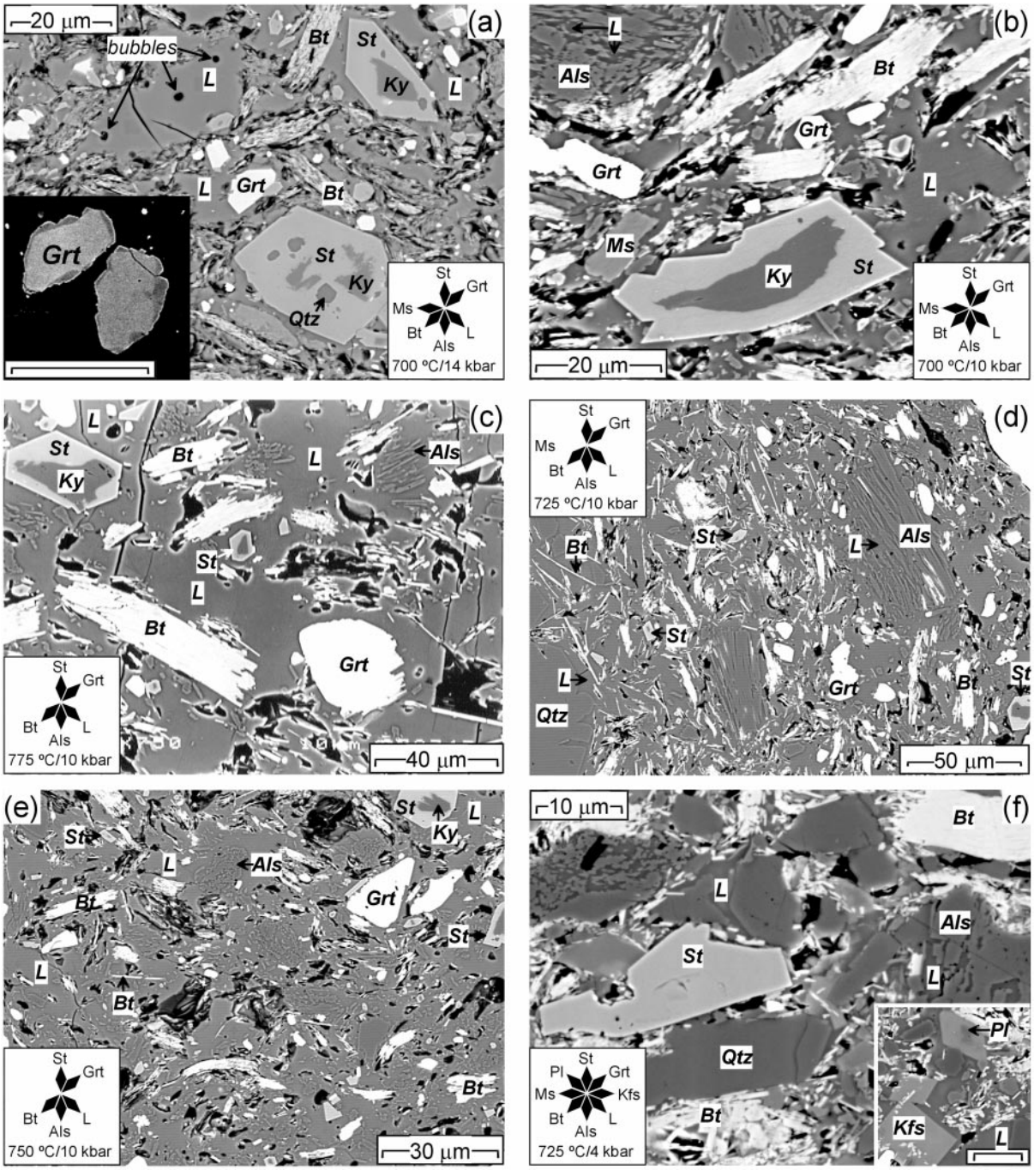

Fig. 3. Back-scattered electron images of St-bearing run products. (a)–(e) Fluid-present and (f) fluid-absent runs. Note the systematic presence of kyanite relicts within newly formed idiomorphic staurolite in the fluid-present runs, as opposed to the fluid-absent runs, and the dissolution of Al-silicate into the melt in the fluid-present runs. The inset in (a) illustrates coexisting garnet with new composition (richer in Mg) at the rims of the relict grains (scale bar represents 20 μm). The inset in (f) illustrates coexisting K-feldspar that locally includes relict plagioclase (scale bar represents 10 μm).

H_2O-fluid), have been omitted from consideration as their amounts in the intervening phases are inaccurate or unknown. For each model, the rank of the resulting composite reactant + product assemblage matrix is eight, the associated null space (i.e. reaction space) is three-dimensional, and there exist 55 reactions involving rank + 1 phases. Table 8 gives the subsets of reactions out of these 55 reactions that fit the condition of incompatibility among reactants and products (see Fisher, 1989) for experiments at 10 kbar. It should

Table 3: Averages of glass composition ($\pm 1\sigma$) from the fluid-present and fluid-absent experiments normalized to 8-oxygen anhydrous basis and $Fe_{total} = Fe^{2+}$

P (kbar):	6	6	8	10	10	10	10	12	12	14
T (°C):	675	700	725	700	725	750	775	700	725	700
n:	2	6	5	5	8	7	7	7	7	6
Fluid-present experiments										
SiO_2	64·16 (0·11)	65·12 (0·19)	65·01 (1·04)	62·23 (0·60)	63·96 (0·96)	64·51 (0·92)	64·92 (1·53)	63·70 (1·48)	63·93 (1·07)	65·63 (1·15)
TiO_2	0·03 (0·04)	0·08 (0·05)	0·06 (0·10)	0·07 (0·07)	0·10 (0·09)	0·11 (0·09)	0·11 (0·10)	0·10 (0·05)	0·12 (0·13)	0·07 (0·06)
Al_2O_3	14·71 (1·05)	14·53 (0·60)	14·89 (0·57)	14·44 (0·66)	13·63 (0·21)	13·56 (0·18)	13·41 (0·26)	15·61 (0·26)	14·28 (0·20)	14·42 (0·36)
FeO	0·95 (0·08)	1·18 (0·19)	1·24 (0·23)	1·43 (0·28)	1·55 (0·11)	1·62 (0·22)	1·81 (0·12)	1·22 (0·08)	1·39 (0·08)	0·93 (0·20)
MnO	0·06 (0·04)	0·08 (0·10)	0·06 (0·07)	0·08 (0·06)	0·07 (0·07)	0·06 (0·05)	0·06 (0·07)	0·03 (0·04)	0·00 (0·01)	0·03 (0·04)
MgO	0·10 (0·12)	0·12 (0·05)	0·15 (0·09)	0·13 (0·09)	0·26 (0·08)	0·37 (0·06)	0·40 (0·03)	0·18 (0·04)	0·19 (0·07)	0·11 (0·05)
CaO	1·96 (0·49)	2·08 (0·02)	2·50 (0·25)	2·65 (0·12)	2·26 (0·08)	1·90 (0·07)	1·86 (0·08)	2·61 (0·07)	2·20 (0·09)	2·25 (0·06)
Na_2O	2·24 (0·38)	2·06 (0·30)	1·99 (0·25)	2·43 (0·33)	1·92 (0·17)	1·69 (0·13)	1·45 (0·24)	2·65 (0·37)	2·39 (0·31)	3·57 (0·50)
K_2O	2·07 (0·13)	2·38 (0·07)	2·04 (0·09)	1·59 (0·14)	2·13 (0·11)	2·66 (0·08)	2·70 (0·13)	1·17 (0·11)	2·09 (0·05)	1·46 (0·14)
Sum	86·25 (1·80)	87·69 (0·79)	88·03 (1·94)	85·06 (0·58)	85·86 (1·08)	86·48 (1·16)	86·71 (2·17)	87·32 (1·79)	86·74 (1·38)	88·50 (1·76)
Si	3·19 (0·05)	3·19 (0·03)	3·18 (0·02)	3·16 (0·03)	3·21 (0·02)	3·22 (0·01)	3·23 (0·00)	3·13 (0·01)	3·18 (0·01)	3·19 (0·01)
Ti	0·00 (0·00)	0·00 (0·00)	0·00 (0·00)	0·00 (0·00)	0·00 (0·00)	0·00 (0·00)	0·00 (0·00)	0·00 (0·00)	0·00 (0·00)	0·00 (0·00)
Al	0·86 (0·05)	0·84 (0·03)	0·86 (0·02)	0·86 (0·04)	0·81 (0·01)	0·80 (0·01)	0·79 (0·01)	0·91 (0·01)	0·84 (0·02)	0·83 (0·01)
Fe^{2+}	0·04 (0·00)	0·05 (0·01)	0·05 (0·01)	0·06 (0·01)	0·07 (0·01)	0·07 (0·01)	0·08 (0·01)	0·05 (0·00)	0·06 (0·00)	0·04 (0·01)
Mn	0·00 (0·00)	0·00 (0·00)	0·00 (0·00)	0·00 (0·00)	0·00 (0·00)	0·00 (0·00)	0·00 (0·00)	0·00 (0·00)	0·00 (0·00)	0·00 (0·00)
Mg	0·01 (0·01)	0·01 (0·00)	0·01 (0·01)	0·01 (0·01)	0·02 (0·01)	0·03 (0·00)	0·03 (0·00)	0·01 (0·00)	0·01 (0·00)	0·01 (0·00)
Ca	0·10 (0·02)	0·11 (0·00)	0·13 (0·01)	0·14 (0·01)	0·12 (0·00)	0·10 (0·00)	0·10 (0·00)	0·14 (0·00)	0·12 (0·00)	0·12 (0·00)
Na	0·22 (0·03)	0·20 (0·03)	0·19 (0·02)	0·24 (0·03)	0·19 (0·01)	0·16 (0·01)	0·14 (0·02)	0·25 (0·03)	0·23 (0·03)	0·34 (0·05)
K	0·13 (0·01)	0·15 (0·01)	0·13 (0·01)	0·10 (0·01)	0·14 (0·01)	0·17 (0·01)	0·17 (0·00)	0·07 (0·01)	0·13 (0·00)	0·09 (0·01)
Mg#	0·14 (0·17)	0·15 (0·05)	0·17 (0·07)	0·13 (0·07)	0·23 (0·06)	0·29 (0·05)	0·28 (0·02)	0·21 (0·04)	0·19 (0·05)	0·17 (0·09)

Table 3: continued

P (kbar):	4	6	6	6	6	10	10	10
T (°C):	725	750	775	800	825	775	800	825
n:	3	25	6	2	5	3	6	1
Fluid-absent experiments								
SiO_2	68·77 (0·62)	66·10 (2·60)	63·48 (1·61)	66·45 (3·71)	66·66 (1·26)	63·25 (1·75)	63·77 (3·78)	60·48
TiO_2	0·06 (0·06)	0·18 (0·13)	0·20 (0·11)	0·20 (0·01)	0·25 (0·22)	0·14 (0·13)	0·15 (0·14)	0·34
Al_2O_3	13·68 (0·25)	14·30 (0·65)	14·74 (0·90)	15·61 (1·76)	13·56 (0·34)	16·99 (0·39)	16·40 (2·22)	16·81
FeO	1·06 (0·13)	1·61 (0·57)	1·81 (0·61)	1·78 (0·34)	1·58 (0·28)	1·22 (0·15)	1·32 (0·35)	2·19
MnO	0·13 (0·08)	0·08 (0·06)	0·03 (0·03)	0·13 (0·01)	0·05 (0·09)	0·06 (0·11)	0·05 (0·06)	0
MgO	0·06 (0·03)	0·41 (0·31)	0·54 (0·26)	0·39 (0·34)	0·21 (0·09)	0·25 (0·20)	0·28 (0·30)	0·66
CaO	0·58 (0·03)	0·80 (0·10)	0·84 (0·03)	0·77 (0·02)	0·78 (0·03)	0·78 (0·12)	0·71 (0·09)	0·63
Na_2O	1·43 (0·10)	1·62 (0·28)	1·55 (0·20)	1·89 (0·76)	2·42 (0·07)	2·10 (0·44)	1·96 (0·36)	1·82
K_2O	3·89 (0·53)	4·04 (0·52)	4·01 (0·60)	4·37 (0·80)	4·41 (0·16)	3·21 (0·12)	3·38 (0·39)	4·57
Sum	89·70 (0·53)	89·13 (2·26)	87·20 (1·25)	91·56 (2·80)	89·93 (1·71)	87·99 (1·64)	88·15 (0·91)	87·81
Si	3·29 (0·01)	3·21 (0·06)	3·16 (0·05)	3·16 (0·09)	3·23 (0·01)	3·10 (0·03)	3·12 (0·13)	3·03
Ti	0·00 (0·00)	0·01 (0·00)	0·01 (0·00)	0·01 (0·00)	0·01 (0·01)	0·01 (0·00)	0·01 (0·01)	0·01
Al	0·77 (0·02)	0·82 (0·04)	0·87 (0·04)	0·88 (0·12)	0·77 (0·01)	0·98 (0·04)	0·95 (0·14)	0·99
Fe^{2+}	0·04 (0·01)	0·07 (0·02)	0·08 (0·03)	0·07 (0·02)	0·06 (0·01)	0·05 (0·01)	0·05 (0·02)	0·09
Mn	0·01 (0·00)	0·00 (0·00)	0·00 (0·00)	0·01 (0·00)	0·00 (0·00)	0·00 (0·00)	0·00 (0·00)	0
Mg	0·00 (0·00)	0·03 (0·02)	0·04 (0·02)	0·03 (0·02)	0·02 (0·01)	0·02 (0·01)	0·02 (0·02)	0·05
Ca	0·03 (0·00)	0·04 (0·01)	0·05 (0·00)	0·04 (0·00)	0·04 (0·00)	0·04 (0·01)	0·04 (0·00)	0·03
Na	0·13 (0·01)	0·15 (0·02)	0·15 (0·02)	0·17 (0·07)	0·23 (0·01)	0·20 (0·04)	0·19 (0·03)	0·18
K	0·24 (0·03)	0·25 (0·03)	0·25 (0·04)	0·26 (0·04)	0·27 (0·00)	0·20 (0·00)	0·21 (0·03)	0·29
Mg#	0·09 (0·05)	0·27 (0·11)	0·33 (0·07)	0·25 (0·15)	0·19 (0·09)	0·24 (0·12)	0·21 (0·18)	0·35

Table 4: Averages of staurolite composition ($\pm 1\sigma$) normalized to 48 oxygens, $Si + Al + 2/3Ti + Fe^{3+} = 25{\cdot}55$, and $Fe^{3+} = 3{\cdot}5\%$ of Fe_{total} (Holdaway et al., *1991, 1995)*

P (kbar):	6	8	10	10	10	10	12	12	14	4	6
T (°C):	700	725	700	725	750	775	700	725	700	725	825
wt % H_2O:	10	10	10	10	10	10	10	10	10	0	0
n:	4	8	6	3	5	5	2	7	6	1	2
SiO_2	25·97 (0·21)	26·98 (0·86)	26·36 (0·39)	26·04 (0·65)	26·40 (0·81)	26·17 (0·51)	26·89 (0·27)	27·23 (0·51)	27·25 (0·51)	26·99	25·83 (0·38)
TiO_2	0·55 (0·10)	0·74 (0·17)	0·60 (0·16)	0·84 (0·13)	0·79 (0·15)	0·98 (0·17)	0·80 (0·27)	0·80 (0·10)	0·69 (0·18)	0·65	0·56 (0·16)
Al_2O_3	54·84 (1·00)	55·06 (1·28)	53·51 (1·23)	54·04 (0·57)	53·38 (1·09)	53·65 (0·81)	53·87 (1·58)	54·39 (0·75)	53·96 (0·60)	52·02	54·21 (0·81)
FeO	12·28 (0·65)	12·12 (0·44)	12·53 (0·17)	13·55 (0·25)	13·65 (0·32)	13·59 (0·28)	13·43 (0·61)	12·91 (0·66)	12·85 (0·36)	12·1	13·64 (0·10)
MnO	0·15 (0·18)	0·18 (0·10)	0·20 (0·07)	0·16 (0·02)	0·19 (0·09)	0·18 (0·10)	0·12 (0·05)	0·16 (0·06)	0·12 (0·11)	0·36	0·19 (0·00)
ZnO	1·09 (0·33)	0·76 (0·28)	1·58 (0·17)	1·35 (0·32)	1·18 (0·37)	0·84 (0·12)	0·67 (0·41)	0·57 (0·30)	0·66 (0·18)	1·54	0·59 (0·07)
MgO	1·61 (0·17)	1·83 (0·38)	2·04 (0·09)	1·81 (0·17)	1·98 (0·20)	1·95 (0·20)	1·99 (0·18)	2·03 (0·17)	2·21 (0·21)	1·54	2·58 (0·04)
Sum	96·47 (1·19)	97·67 (1·53)	96·83 (1·29)	97·80 (0·63)	97·57 (0·50)	97·40 (0·92)	97·76 (0·71)	98·10 (0·93)	97·73 (0·59)	95·2	97·59 (1·36)
Si	7·27 (0·07)	7·45 (0·18)	7·48 (0·16)	7·35 (0·16)	7·49 (0·27)	7·41 (0·15)	7·54 (0·19)	7·55 (0·15)	7·60 (0·15)	7·75	7·30 (0·01)
Ti	0·12 (0·02)	0·15 (0·03)	0·13 (0·03)	0·18 (0·03)	0·17 (0·03)	0·21 (0·04)	0·17 (0·06)	0·17 (0·02)	0·15 (0·04)	0·14	0·12 (0·03)
Al	18·10 (0·08)	17·91 (0·17)	17·88 (0·14)	17·97 (0·14)	17·84 (0·26)	17·89 (0·14)	17·79 (0·24)	17·78 (0·14)	17·75 (0·13)	17·6	18·06 (0·01)
Fe^{3+}	0·10 (0·01)	0·10 (0·01)	0·10 (0·00)	0·11 (0·00)	0·11 (0·00)	0·11 (0·00)	0·11 (0·01)	0·10 (0·01)	0·10 (0·00)	0·1	0·11 (0·00)
Fe^{2+}	2·78 (0·14)	2·70 (0·15)	2·87 (0·06)	3·09 (0·07)	3·12 (0·07)	3·10 (0·04)	3·04 (0·19)	2·89 (0·15)	2·89 (0·08)	2·8	3·11 (0·07)
Mn	0·04 (0·04)	0·04 (0·02)	0·05 (0·02)	0·04 (0·01)	0·05 (0·02)	0·04 (0·02)	0·03 (0·01)	0·04 (0·01)	0·03 (0·03)	0·09	0·05 (0·00)
Zn	0·23 (0·07)	0·16 (0·06)	0·33 (0·04)	0·28 (0·07)	0·25 (0·08)	0·18 (0·02)	0·14 (0·08)	0·12 (0·06)	0·14 (0·04)	0·33	0·12 (0·01)
Mg	0·67 (0·06)	0·75 (0·15)	0·86 (0·05)	0·76 (0·07)	0·84 (0·09)	0·82 (0·09)	0·83 (0·09)	0·84 (0·07)	0·92 (0·09)	0·66	1·08 (0·00)
H	4·44 (0·31)	4·30 (0·39)	3·39 (0·26)	3·31 (0·32)	3·02 (0·52)	3·22 (0·21)	3·41 (0·67)	3·69 (0·40)	3·50 (0·23)	3·56	3·09 (0·06)
Mg#	0·19 (0·01)	0·22 (0·03)	0·23 (0·01)	0·20 (0·02)	0·21 (0·02)	0·21 (0·02)	0·21 (0·01)	0·23 (0·01)	0·24 (0·02)	0·19	0·26 (0·00)

n, number of analyses.

Table 5: Composition of biotite with the highest Mg# in each run (normalized to 22 oxygens, $Fe_{total} = Fe^{2+}$)

P (kbar):	10	10	10	10	6	6	6	6	6	10
T (°C):	700	725	750	775	750	775	800	825	850	775
wt % H_2O:	10	10	10	10	0	0	0	0	0	0
SiO_2	35·43	36·85	37·15	37·03	35·45	35·25	34·75	34·85	35·95	35·22
TiO_2	2·57	2·00	2·77	2·83	0·70	3·26	2·96	2·70	3·57	3·06
Al_2O_3	20·83	20·56	20·49	18·94	21·43	20·31	20·42	19·78	19·76	21·43
FeO	18·87	19·86	19·63	18·42	19·45	20·76	19·85	17·90	13·63	19·67
MnO	0·00	0·16	0·12	0·17	0·27	0·14	0·11	0·00	0·08	0·00
MgO	7·79	8·03	8·06	8·25	9·10	7·01	6·89	9·98	12·75	7·90
CaO	0·00	0·00	0·00	0·00	0·00	0·00	0·00	0·00	0·00	0·00
Na_2O	0·65	0·63	0·52	0·68	0·18	0·42	0·52	0·58	0·42	0·74
K_2O	8·44	8·32	8·28	8·11	8·49	8·97	8·42	8·36	8·92	8·64
Sum	94·68	96·91	97·02	94·43	95·07	96·12	93·92	94·15	95·08	96·66
Si	5·37	5·48	5·48	5·60	5·36	5·33	5·35	5·31	5·32	5·26
Ti	0·29	0·22	0·31	0·32	0·08	0·37	0·34	0·31	0·40	0·34
Al	3·72	3·60	3·57	3·38	3·82	3·62	3·71	3·55	3·44	3·77
Fe^{2+}	2·39	2·47	2·42	2·33	2·46	2·63	2·56	2·28	1·69	2·46
Mn	0·00	0·02	0·02	0·02	0·03	0·02	0·01	0·00	0·01	0·00
Mg	1·76	1·78	1·77	1·86	2·05	1·58	1·58	2·27	2·81	1·76
Ca	0·00	0·00	0·00	0·00	0·00	0·00	0·00	0·00	0·00	0·00
Na	0·19	0·18	0·15	0·20	0·05	0·12	0·16	0·17	0·12	0·21
K	1·63	1·58	1·56	1·56	1·64	1·73	1·65	1·62	1·68	1·65
Mg#	0·42	0·42	0·42	0·44	0·45	0·38	0·38	0·50	0·63	0·42

be noted that, because the reaction space is three-dimensional, three linearly independent reactions from each subset in Table 8 are sufficient to describe the reaction space of the models. The bulk mass-balance equation implied in each experiment can be obtained by linear combination of the three selected reactions. For this task, however, it is needed to weight the three selected reactions, and this can be done only if the relative volume (or molar) amounts of reactant and product phases or compositions are known. The precise estimation of the amounts of reactant and product biotite by means of image analysis is hampered by their virtually indistinguishable shade of grey in the back-scattered electron images, and the same applies for garnet. Thus, a bulk mass-balance equation cannot be given. However, because the coefficients of all the reactions in the subsets of Table 8 consistently indicate a net consumption of Al-silicate, garnet and biotite, and a production of staurolite and melt, the bulk mass-balance equations probably take the form

$$\mathrm{Qtz} + \mathrm{Pl} + \mathrm{Ms} + \mathrm{Bt} + \mathrm{Grt} + \mathrm{Als} + \mathrm{V} = \mathrm{St} + \mathrm{L}. \quad (1)$$

This generalized reaction agrees with the textural observation of the predominance of the relict grains/compositions of biotite and garnet over the newly formed ones, and suggests that the latter formed as a response to equilibration of the dissolving grains of the former. The observed sequence of Fe–Mg partitioning and the reaction relationships implied in the AFM diagram of Fig. 1e also indicate a net consumption of garnet and biotite (i.e. Grt + Bt + Als = St + L), and do not conform with a net production of garnet (i.e. Bt + Als = Grt + St + L). This point is discussed in more detail below.

Fluid-absent experiments

The first melts formed at 725°C, 6 kbar and 775°C, 10 kbar, indicating a fluid-absent solidus curve located at higher temperature and with flatter positive dP/dT slope than the fluid-present solidus, as expected (Fig. 2; Lambert *et al.*, 1969; Thompson & Algor, 1977; Vielzeuf & Schmidt, 2001). At low temperature (<800°C), the most prominent feature is the formation of Al-silicate and K-feldspar as a result of melting reactions controlled mostly by Ms + Qtz breakdown.

Table 6: Composition of garnet rims with the highest Mg# (normalized to 12 oxygens, $Fe_{total} = Fe^{2+}$)

P (kbar):	6	8	10	10	10	10	12	12	14	6	6	6	6	6	10	10	10
T (°C):	700	725	700	725	750	775	700	725	700	750	775	800	825	850	775	800	825
wt % H_2O:	10	10	10	10	10	10	10	10	10	0	0	0	0	0	0	0	0
SiO_2	37·36	37·16	37·44	36·87	37·46	37·03	38·43	37·18	37·02	37·80	36·97	36·39	39·68	37·45	36·96	36·16	37·90
TiO_2	0·07	0·13	0·00	0·11	0·30	0·31	0·40	0·69	0·40	0·00	0·08	0·00	0·53	0·53	0·47	0·53	0·35
Al_2O_3	21·50	21·65	21·83	21·82	22·00	19·94	21·70	21·92	21·15	21·67	21·00	20·95	22·73	21·70	21·18	21·48	23·73
FeO	29·21	31·41	32·70	35·17	33·18	31·95	27·53	30·32	28·68	32·95	34·24	34·62	29·94	30·76	31·12	30·78	28·26
MnO	4·08	4·52	1·43	1·95	1·75	1·47	1·49	0·92	0·61	2·45	0·49	1·96	0·80	0·56	2·65	2·44	1·78
MgO	2·73	2·62	2·93	3·44	3·70	3·75	2·51	3·72	3·19	3·27	2·88	2·65	5·61	7·05	3·85	3·43	3·91
CaO	3·74	2·45	3·08	1·47	2·07	1·88	6·51	3·83	6·33	2·94	4·25	2·78	1·56	1·80	4·53	4·51	3·82
Sum	99·11	99·97	99·95	100·83	100·46	96·65	98·57	98·58	97·38	101·08	99·91	99·35	100·85	99·85	100·76	99·33	99·75
Si	3·01	2·98	2·99	2·94	2·97	3·05	3·06	2·98	3·00	2·99	2·98	2·96	3·05	2·94	2·94	2·92	2·97
Ti	0·00	0·01	0·00	0·01	0·02	0·02	0·02	0·04	0·02	0·00	0·00	0·00	0·03	0·03	0·03	0·03	0·02
Al	2·04	2·05	2·06	2·05	2·06	1·94	2·03	2·07	2·02	2·02	1·99	2·01	2·06	2·01	1·98	2·04	2·19
Fe^{2+}	1·97	2·11	2·19	2·35	2·20	2·20	1·83	2·03	1·94	2·18	2·30	2·36	1·92	2·02	2·07	2·08	1·85
Mn	0·28	0·31	0·10	0·13	0·12	0·10	0·10	0·06	0·04	0·16	0·03	0·14	0·05	0·04	0·18	0·17	0·12
Mg	0·33	0·31	0·35	0·41	0·44	0·46	0·30	0·44	0·39	0·39	0·35	0·32	0·64	0·83	0·46	0·41	0·46
Ca	0·32	0·21	0·26	0·13	0·18	0·17	0·55	0·33	0·55	0·25	0·37	0·24	0·13	0·15	0·39	0·39	0·32
Mg#	0·14	0·13	0·14	0·15	0·17	0·17	0·14	0·18	0·17	0·15	0·13	0·12	0·25	0·29	0·18	0·17	0·20

Table 7: Composition of plagioclase with maximum An content and average K-feldspar ($\pm 1\sigma$) normalized to 8 oxygens and $Fe_{total} = Fe^{3+}$ from the fluid-absent runs

	Pl								Kfs				
P (kbar):	4	6	6	6	6	6	10	10	4	6	6	10	10
T (°C):	725	750	775	800	825	850	775	800	725	750	850	775	825
n:									4	9	2	1	2
SiO_2	61·04	56·08	59·71	57·77	55·13	61·31	58·44	58·45	64·44 (0·48)	62·59 (0·89)	64·50 (0·04)	62·8	66·00 (1·13)
Al_2O_3	24·63	27·87	24·5	27·54	28·44	24·89	25·72	26·09	19·14 (0·20)	20·37 (0·66)	19·20 (0·04)	21·27	18·68 (0·69)
FeO	0·14	0·68	0·29	0·34	0·13	0·29	0·36	0·14	0·25 (0·04)	0·88 (0·91)	0·42 (0·05)	0·55	0·13 (0·18)
CaO	5·55	9·02	6·02	7·66	8·66	6·26	7·19	8·27	0·05 (0·03)	0·15 (0·12)	0·35 (0·08)	0·03	0·09 (0·01)
Na_2O	7·14	5·12	7·17	5·33	5·53	7·31	6·45	6·46	1·86 (0·19)	1·74 (0·21)	2·54 (0·13)	2·35	2·34 (0·01)
K_2O	1·53	0·93	0·93	0·96	0·69	0·76	1	0·56	12·91 (0·25)	12·67 (0·40)	11·75 (0·29)	11·88	11·73 (1·00)
Sum	100·03	99·7	98·62	99·6	98·58	100·82	99·16	99·97	98·58 (0·56)	98·37 (0·61)	98·75 (0·06)	98·88	98·97 (0·74)
Si	2·72	2·53	2·7	2·59	2·51	2·71	2·64	2·62	2·98 (0·01)	2·91 (0·04)	2·97 (0·00)	2·89	3·02 (0·05)
Al	1·29	1·48	1·3	1·45	1·53	1·29	1·37	1·38	1·04 (0·01)	1·12 (0·03)	1·04 (0·00)	1·15	1·01 (0·04)
Fe^{3+}	0·01	0·03	0·01	0·01	0	0·01	0·01	0·01	0·01 (0·00)	0·03 (0·04)	0·02 (0·00)	0·02	0·00 (0·01)
Ca	0·26	0·44	0·29	0·37	0·42	0·3	0·35	0·4	0·00 (0·00)	0·01 (0·01)	0·02 (0·00)	0	0·00 (0·00)
Na	0·62	0·45	0·63	0·46	0·49	0·63	0·56	0·56	0·17 (0·02)	0·16 (0·02)	0·23 (0·01)	0·21	0·21 (0·00)
K	0·09	0·05	0·05	0·05	0·04	0·04	0·06	0·03	0·76 (0·02)	0·75 (0·03)	0·69 (0·02)	0·7	0·68 (0·06)

n, number of analyses.

Table 8: Sets of coefficients (in molar units, normalized to 1 mole of melt) of incompatibility reactions among the reactants and products (out of a total of 55 possible reactions for each set) for the three fluid-present experiments with $Mg\#^{Grt} < Mg\#^{St} < Mg\#^{L} < Mg\#^{Bt}$ *at 10 kbar (calculated using* CSpace, *Torres-Roldán* et al., *2000)*

	Reactant assemblage							Product assemblage				Net balance	
T (°C)	Als	Bt	Grt	Ilm	Ms	Pl	Qtz	Melt	Bt	Grt	St	ΔBt*	ΔGrt*
725	−1·333	−0·139	−0·184	0·000	0·000	−0·269	−1·403	1·000	0·071	0·027	0·152	−0·068	−0·157
725	−0·653	−0·042	−0·250	0·000	−0·035	−0·254	−1·660	1·000	0·000	0·162	0·073	−0·042	−0·089
725	−1·438	−0·134	−0·174	−0·001	0·000	−0·268	−1·348	1·000	0·064	0·000	0·166	−0·069	−0·174
725	−1·338	−0·054	−0·185	−0·006	−0·022	−0·256	−1·340	1·000	0·000	0·000	0·159	−0·054	−0·185
750	−0·950	−0·062	−0·198	0·000	−0·034	−0·218	−1·604	1·000	0·000	0·085	0·112	−0·062	−0·113
750	−1·295	−0·148	−0·142	0·000	−0·008	−0·229	−1·508	1·000	0·069	0·000	0·150	−0·079	−0·142
750	−1·123	−0·060	−0·151	−0·002	−0·036	−0·218	−1·502	1·000	0·000	0·000	0·136	−0·060	−0·151
775	−1·073	−0·136	−0·247	0·000	0·000	−0·196	−1·750	1·000	0·045	0·166	0·117	−0·091	−0·081
775	−0·864	−0·075	−0·271	0·000	−0·022	−0·186	−1·788	1·000	0·000	0·194	0·096	−0·075	−0·076
775	−1·485	−0·148	−0·157	−0·004	0·000	−0·198	−1·510	1·000	0·058	0·000	0·171	−0·090	−0·157
775	−1·296	−0·067	−0·169	−0·006	−0·031	−0·185	−1·504	1·000	0·000	0·000	0·155	−0·067	−0·169

*Product + reactant biotite and garnet.

At higher temperature, widespread instability of biotite led to noticeable amounts of newly formed garnet, particularly at 10 kbar, whereas hercynite formed at 825 and 850°C, 6 kbar. Muscovite persisted within the range 725–825°C, even at conditions of formation of hercynite.

Staurolite formed in fluid-absent runs at 725°C, 4 kbar, and 825°C, 6 kbar (Table 2, Figs 2 and 3f). It has an idiomorphic shape and is surrounded by melt but, at variance with the fluid-present experiments, staurolite from these fluid-absent runs formed sporadically, does not contain kyanite cores, and coexists with K-feldspar.

Phase compositions

All the melts formed in the fluid-present and fluid-absent experiments are granitic *sensu lato*, with 61·39–67·51 and 59·24–69·93 wt % SiO_2 (wt % not normalized to 100 wt % anhydrous basis), respectively, and have moderately to strongly peraluminous character, with 1·12–1·66 and 1·28–2·36 molar Al/(2Ca + Na + K), respectively. The fluid-present melts are richer in albite and anorthite components, whereas fluid-absent melts are richer in orthoclase (Fig. 4). Where it persists, muscovite does not differ in composition from that of the starting material. In the fluid-present experiments the composition of plagioclase (persisting just above the solidus at 675°C) does not differ from that of the starting material. In the fluid-absent experiments, the composition of rims of plagioclase differs slightly from that of the starting material, trending toward somewhat higher anorthite and orthoclase contents (see Fig. 8b, below). K-feldspar from the fluid-absent experiments has moderate albite content (X_{ab} ~0·2; Fig. 8a and b). The composition of garnet rims departs from the composition of

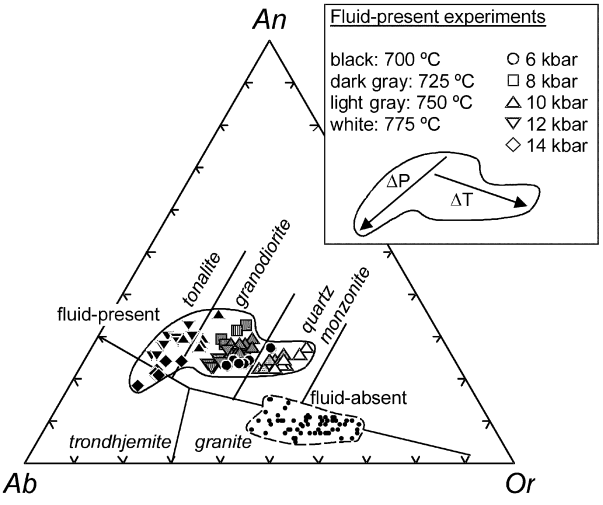

Fig. 4. Normative feldspar end-member contents (wt %) of experimental glasses. It should be noted that the fluid-present melt trends towards trondhjemitic compositions with increasing pressure (at constant *T*), and becomes richer in orthoclase component with rising temperature (at constant *P*). Fields after Barker (1979).

garnet in the starting material in having higher pyrope, Mg# [molar ratio Mg/(Mg + Fe)] and grossular contents (see Fig. 6a and b). The newly formed grains of biotite have higher Mg, Mg# and Ti than the starting material (Fig. 6c and d). The composition of staurolite differs from metamorphic staurolite in other samples from the same outcrop as IJ44, having higher Ti, Mg and Zn, and lower Fe^{2+} (see Fig. 7).

INDICATIONS OF EQUILIBRIUM

Compared with other experimental studies, the most prominent feature of our experiments is the systematic growth of staurolite in the fluid-present runs, a result that suggests the stability of staurolite above the fluid-present solidus of metapelites. This statement, however, critically depends on the extent of equilibrium attained. In the absence of reversed experiments, necessary criteria for an approach to equilibrium are: homogeneity of phase composition, homogeneity of assemblage, and phase rule constraints (see Carrington & Harley, 1995). As in other experimental studies that used natural material, our fluid-present experiments do not fully satisfy these criteria because of important kinetic effects that permitted the persistence of reactant phases and the development of chemical heterogeneities. However, the changes in the relict assemblages are systematic (plagioclase is exhausted adjacent to the solidus, followed by exhaustion of muscovite, and consumption of quartz, Al-silicate, garnet and biotite), and the newly formed assemblage is homogeneous (i.e. St + L, Table 8). Such systematic changes conform with expectations of moving towards equilibrium in the composite reactant–product assemblages. Regular trends in the composition of individual phases and in the partition of elements among the coexisting phases with temperature and pressure are also indications of approach to equilibrium. Below, we evaluate these trends and their degree of consistency with other experiments and natural observations.

Trends in phase composition

Melt

Pressure, temperature and the amount of available H_2O clearly control the composition of the melts formed. The fluid-present melts are poorer in K and Al and richer in Na and Ca (Figs 4 and 5), as expected from the relative contributions of plagioclase (more important in the fluid-present experiments) and muscovite (more important in the fluid-absent experiments). This behaviour is observed at constant P–T for varying amount of added H_2O (i.e. 10 vs 0 wt % added H_2O at 775°C, 10 kbar, Fig. 5). Also, Fe and Mg decrease with decreasing amounts of available H_2O at 775°C, 10 kbar (Fig. 5). These trends argue in favour of the control of the extent of saturation in H_2O on melt composition, as indicated, for example, by Conrad *et al.* (1988), Patiño Douce (1996), Patiño Douce & Harris (1998) and Castro *et al.* (2000).

The melt formed in the fluid-present experiments becomes richer in K and poorer in Ca and Na as temperature rises at constant pressure (Figs 4 and 5; Patiño Douce & Harris, 1998). This trend is a consequence of the increasing contribution of reactant muscovite and biotite as temperature rises. Also, Mg and Mg# increase with rise in temperature (Conrad *et al.*, 1988; Johannes & Holtz, 1996). With increasing pressure, Na increases and K decreases (Figs 4 and 5; Patiño Douce, 1996, 1999; Patiño Douce & Harris, 1998; Castro *et al.*, 1999), indicating increasing contribution of reactant plagioclase relative to muscovite. The trends of Si, Al, Fe, Mg# and Ca apparently suffer inflections or 'jumps' when the Ky–Sil boundary is intersected (Fig. 5). This behaviour is well known in phases present in subsolidus assemblages that contain Al-silicate, and must also apply to supersolidus assemblages (see Spear *et al.*, 1999). However, we acknowledge that the reported inflections or jumps may be apparent because of problems with the precise analysis of the melt. For this reason, and to avoid unjustified speculation, we have centred our attention on compositional changes within the kyanite field only. Within this field, Mg# increases and Ca, Fe and Mg decrease as pressure increases (Fig. 5; Patiño Douce, 1996). This decrease in Fe and Mg is consistent with other experimental results performed at higher temperature, and the increase in Mg# is consistent with expectations of melts coexisting with garnet and biotite (Patiño Douce & Beard, 1995; Patiño Douce, 1996).

The melt formed in the fluid-absent experiments has higher K, Fe, Mg and Mg#, and lower Ca (and Na?) as temperature rises at constant pressure (Fig. 5), and higher Al, Na and Mg#, and lower Si and K with increasing pressure at constant temperature, in agreement with other experimental results (Conrad *et al.*, 1988; Johannes & Holtz, 1996; Pickering & Johnston, 1998; Castro *et al.*, 1999).

Garnet

Pyrope contents and Mg# of the garnet rims increase with rise in temperature, with the larger deviations observed in the fluid-absent experiments because of the higher temperatures attained. Grossular (and to some extent pyrope and Mg#) contents increase with pressure, with the larger deviations acquired in the fluid-present experiments because of the higher pressures attained (Fig. 6a and b). This behaviour is consistent with other experiments, theoretical calculations,

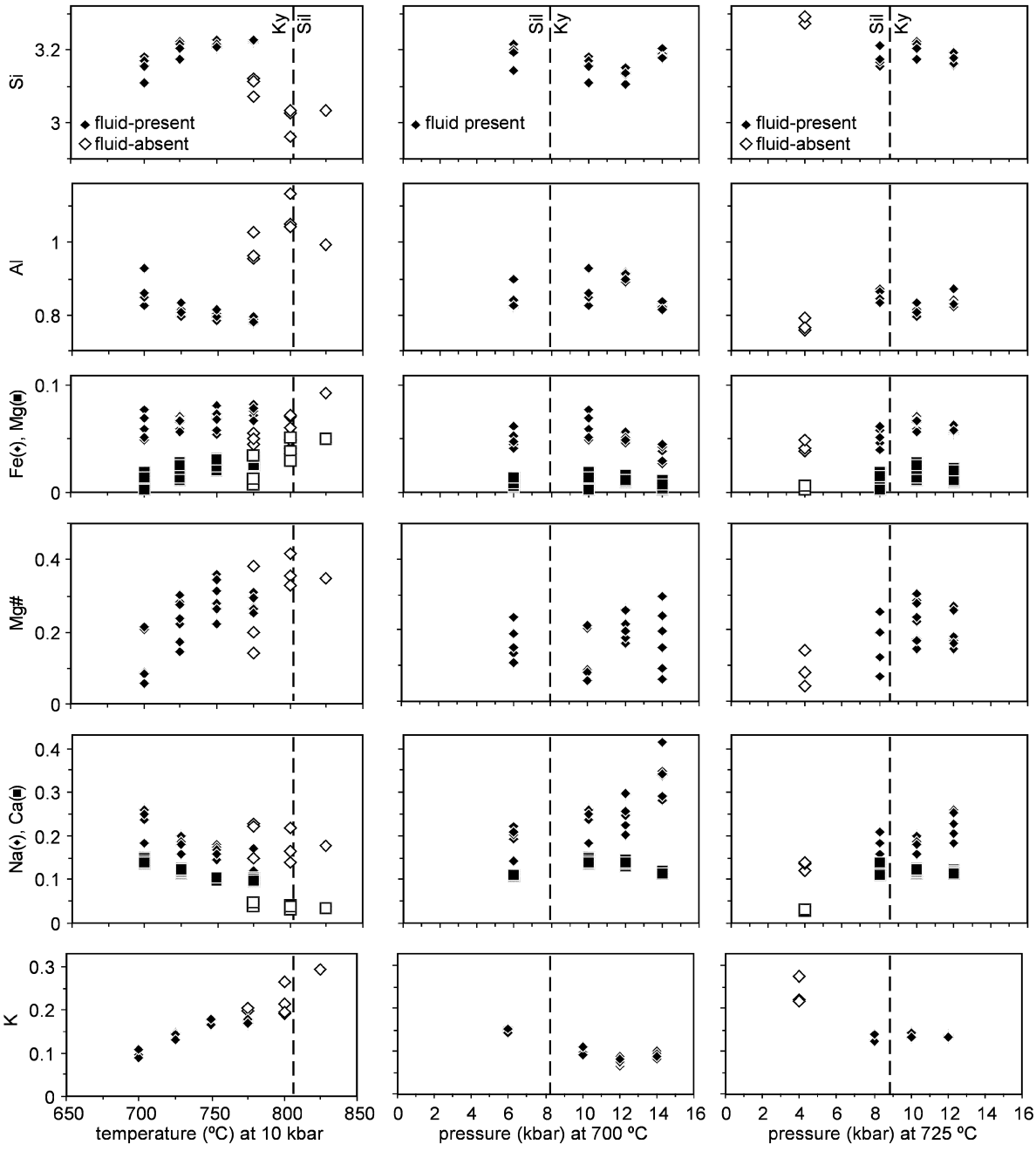

Fig. 5. Variation of composition of experimental glasses (normalized to an H_2O-free eight-oxygen basis) with temperature at 10 kbar and with pressure at 700 and 725°C.

and natural evidence (e.g. Patiño Douce, 1996; Spear *et al.*, 1999; and references therein).

Biotite

No effect of pressure on biotite composition has been noted, although Mg, Mg# and Ti increase with rise in temperature (Fig. 6c and d) in agreement with expectations (e.g. Patiño Douce, 1993; Patiño Douce & Beard, 1996; Pickering & Johnston, 1998). In the fluid-present runs, this trend is observed at 750 and 775°C, whereas in the fluid-absent runs it is manifest at 825 and 850°C.

Staurolite

The formula of staurolite has been calculated following Holdaway *et al.* (1991, 1995). In the fluid-present runs,

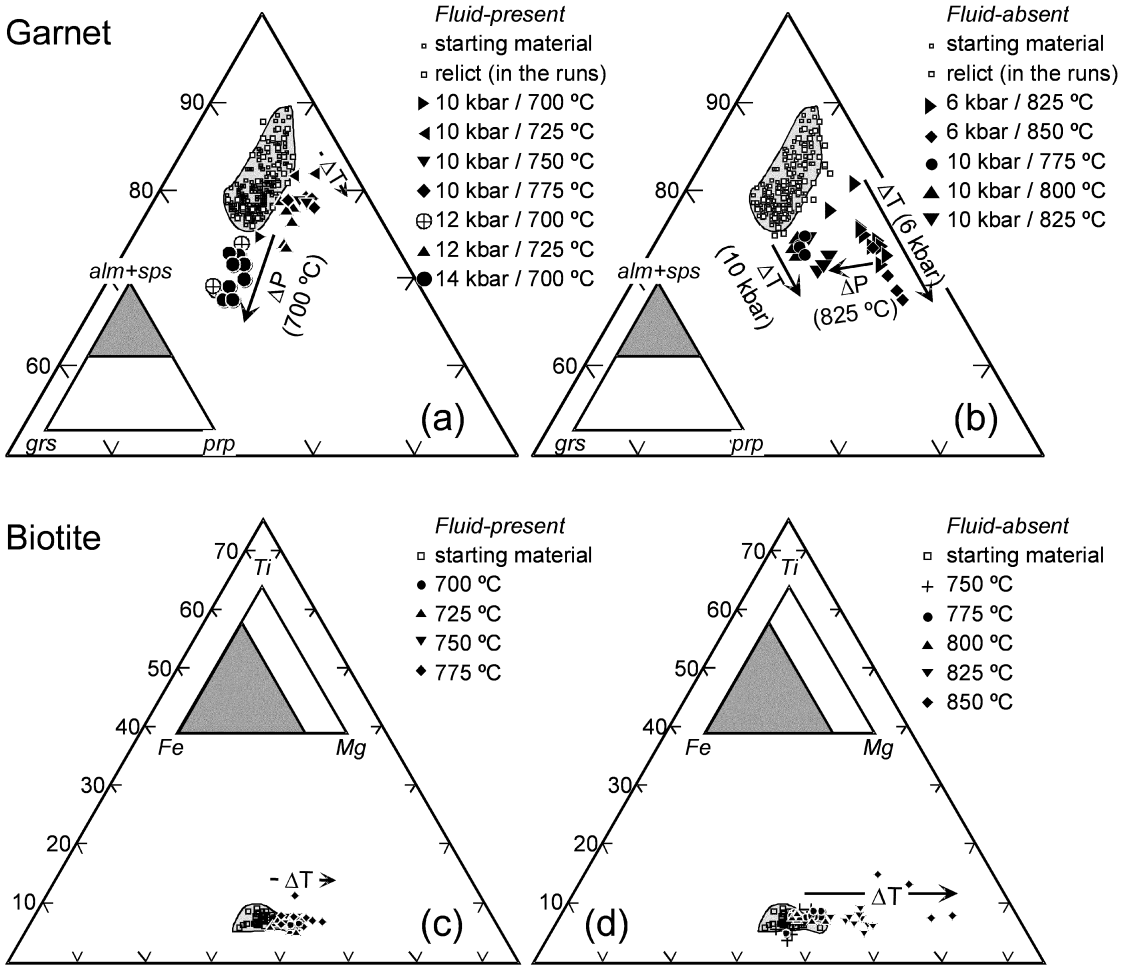

Fig. 6. Variation of composition of (a, b) garnet rims and (c, d) newly formed biotite laths from the fluid-present and fluid-absent runs. Also plotted are the compositions of both phases from the starting material (shaded areas) and of relict grains present in the run products.

Fe^{2+}, Fe^{3+} and Ti increase, and Mg, Mg#, Zn and H decrease with rise in temperature at constant pressure, and Al decreases and Mg, Mg# and Si increase with rise in pressure at constant temperature (Fig. 7). The decrease in Mg# with rise in temperature and the increase in Mg# and Si with increasing pressure are consistent with the experimental results of Koch-Müller (1997) and the findings of Ballevre *et al.* (1989) and Chopin *et al.* (1991) for natural Fe-rich staurolite. The trend of H with pressure seems to suffer an inflection at the Ky–Sil transition. That the calculated H contents decrease with rise in temperature and increase with pressure within the kyanite field agrees with predictions for subsolidus staurolite from assemblages with garnet and Al-silicate (Holdaway *et al.*, 1995). As in other natural and synthetic staurolite, the variation in H occurs following the substitution vector $^{T2/M4}Fe^{2+P}\square_2{}^{T2/M4}\square_{-1}{}^{P}H_{-2}$ (T2, M4 and P denote sites, and $\square$ stands for vacancy; Holdaway *et al.*, 1991, 1995; Hawthorne, 1995).

The composition of staurolite from the fluid-absent experiments is similar to that of the fluid-present experiments, though its sporadic presence does not allow us to work out compositional trends. It is worth mentioning its high Mg content (and Mg#) at the highest temperature of formation (825°C, 6 kbar, Fig. 7).

K-feldspar

No effect of pressure on the composition of K-feldspar formed in the fluid-absent experiments has been noted, but K decreases and Na increases with rise in temperature (Fig. 8a). Approach to equilibrium among the feldspars at 750°C, 6 kbar is indicated by the match of the composition of coexisting feldspars with the

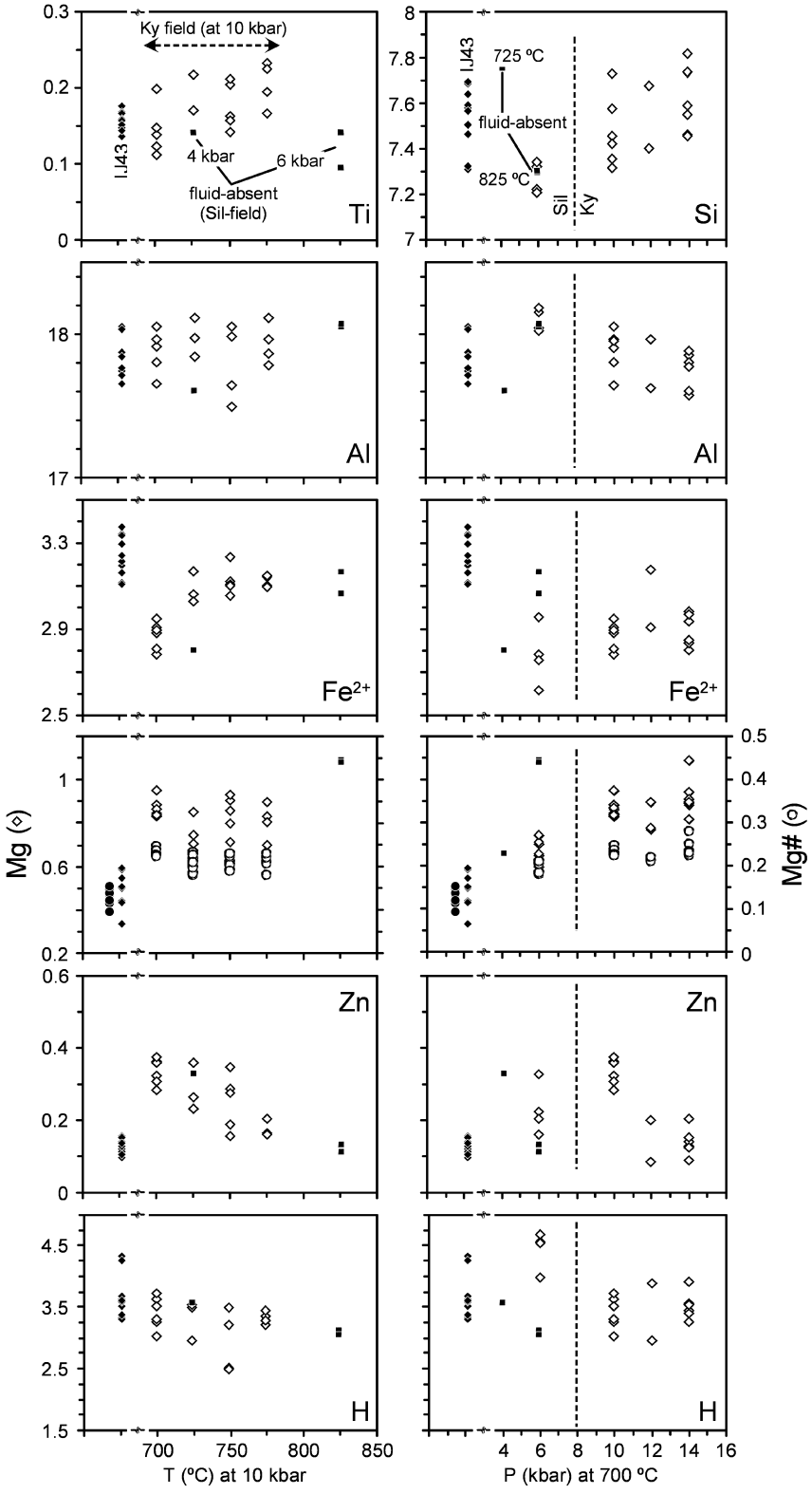

Fig. 7. Variation of composition of staurolite from the fluid-present experiments with temperature at 10 kbar, and with pressure at 700°C. Also plotted is staurolite formed in the fluid-absent experiments (725°C, 4 kbar and 825°C, 6 kbar) and metamorphic staurolite of sample IJ43 taken from the same outcrop as IJ44. Compositions normalized to 48 oxygens and Si + Al + 2/3Ti + Fe^{3+} = 25·55, with Fe^{3+} = 3·5% of Fe_{total} (Holdaway *et al.*, 1991, 1995).

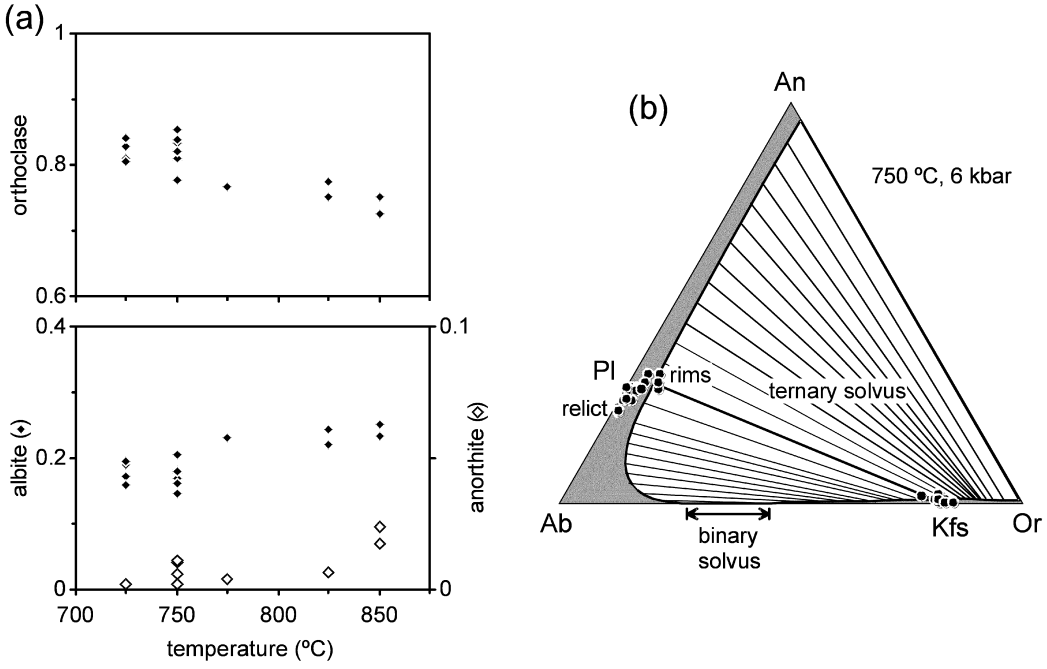

Fig. 8. (a) Variation of composition of K-feldspar with temperature (at all the pressures investigated) from the fluid-absent runs. (b) Composition of plagioclase and K-feldspar from the fluid-absent run at 750°C, 6 kbar in the ternary feldspar triangle contoured with tie-lines joining coexisting feldspars predicted by the solution model of Fuhrman & Lindsley (1988) at the same P and T. The match of the bold tie-line with the experimental run products should be noted (the compositions of plagioclase richer in Na and poorer in K correspond to relict grains present in the runs).

calculated behaviour of the ternary feldspar system using the thermodynamic model of Fuhrman & Lindsley (1988; Fig. 8b).

Fe–Mg partition in the fluid-present runs

For most of the temperature range investigated in the fluid-present runs (i.e. 725–775°C at all pressures), Fe–Mg partitioning among coexisting phases is $Mg\#^{Grt} < Mg\#^{St} < Mg\#^{L} < Mg\#^{Bt}$ (Tables 3–7, Fig. 9a; the compositions of the phases correspond to averages, except for biotite and garnet, which correspond to the compositions with the highest Mg# for each phase to avoid considering relict compositions). However, a reversal between staurolite and liquid (i.e. $Mg\#^{Grt} < Mg\#^{L} < Mg\#^{St} < Mg\#^{Bt}$) takes place at 700°C (at 6, 10, 12 and 14 kbar, Tables 3–7, Fig. 9a). Reversals in Fe–Mg partitioning among coexisting phases as a function of temperature and pressure have been known for a long time and seem to be the rule rather than the exception in supersolidus conditions (Patiño Douce, 1996; García-Casco *et al.*, 2001, and references therein). However, before the relationships among the melt and solid phases are compared with the existing evidence, it is important to inspect the relations among the solid phases.

Staurolite–garnet–biotite partitioning

Our data agree with the relation $Mg\#^{Grt} < Mg\#^{St} < Mg\#^{Bt}$ observed in medium-grade metapelites with low to intermediate Mg# metamorphosed at medium grade and low to intermediate pressure (e.g. Spear & Cheney, 1989; García-Casco & Torres-Roldán, 1996, and references therein). Experiments and occurrences of natural subsolidus assemblages from Fe-rich and Mg-rich rocks have demonstrated the azeotropic behaviour of the Fe–Mg exchange system between staurolite and garnet, that is, a change from normal ($Mg\#^{Grt} < Mg\#^{St}$) to reverse ($Mg\#^{Grt} > Mg\#^{St}$) partitioning in response to increasing Mg# of the system (Saxena, 1973; Rice, 1985; Ganguly & Saxena, 1987; Koch-Müller, 1997), increasing pressure (at least within the kyanite stability field, Ballevere *et al.*, 1989), and rising temperature (Koch-Müller, 1997). Our data confirm these suggestions, as the value of $\ln K_D^{St-Grt}[K_D^{St-Grt} = (Mg/Fe)^{St}/(Mg/Fe)^{Grt}]$ decreases as pressure increases at constant temperature (0·598, 0·483 and 0·437, at 10, 12 and 14 kbar, respectively, 700°C), and as temperature rises at constant pressure (0·598, 0·314, 0·262 and 0·203, at 700, 725, 750 and 775°C, respectively, 10 kbar). The latter trend is apparent in Fig. 9a, where $Mg\#^{Grt}$ and $Mg\#^{St}$ approach each other as temperature rises, and nearly reaches inversion of partitioning at 775°C, 10 kbar.

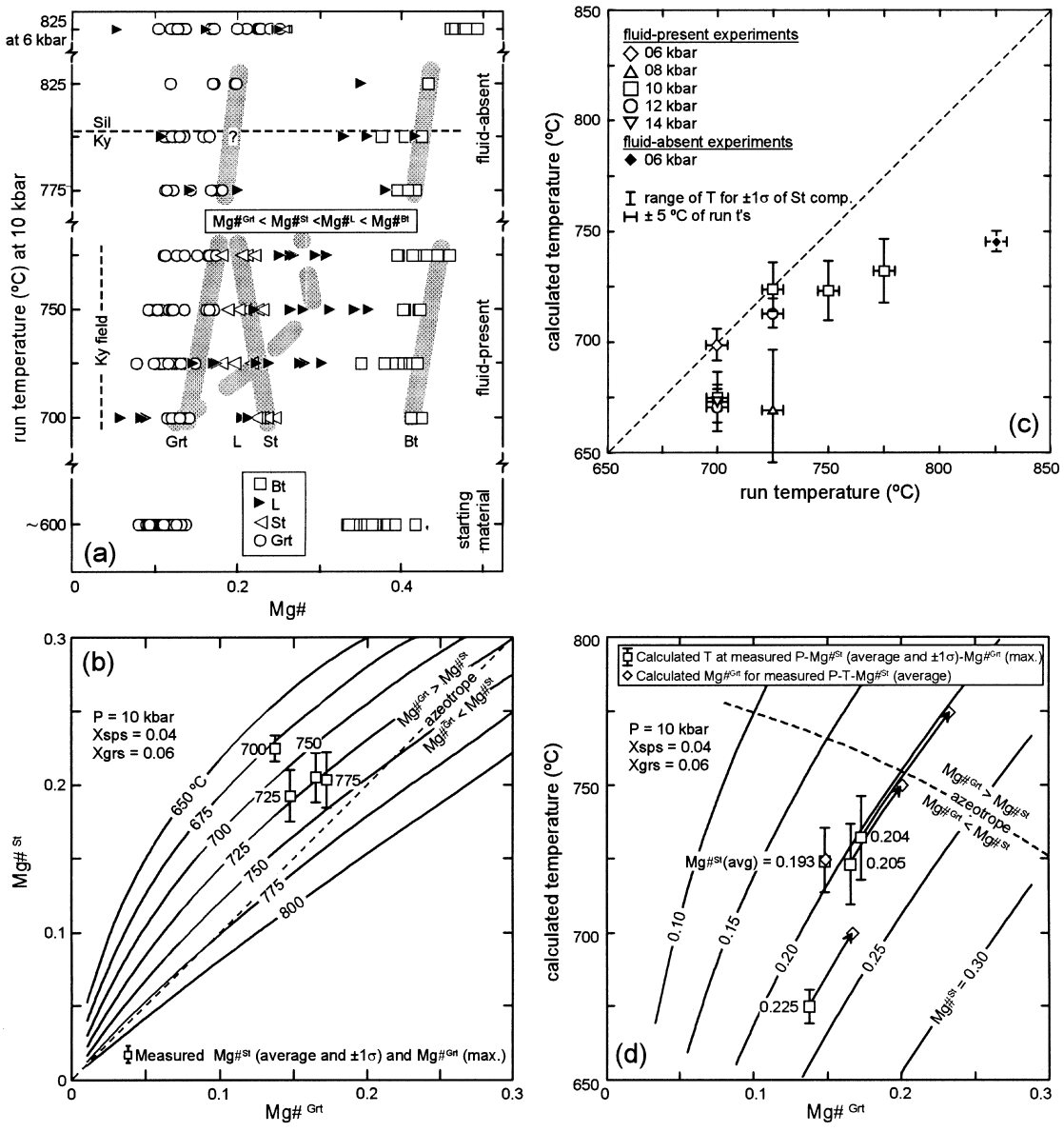

Fig. 9. (a) Variation of Mg# of coexisting phases in the fluid-present and fluid-absent experiments at 10 kbar illustrating Fe–Mg partition. The trends join average compositions (for staurolite and liquid) and the compositions with maximum Mg# (for garnet and biotite). It should be noted that $Mg\#^{Grt}$ and $Mg\#^{St}$ approach each other as temperature rises. For comparison, the fluid-absent staurolite-bearing run at 825°C, 6 kbar is also plotted. (b) Average composition of staurolite (±1σ) vs garnet with maximum Mg# from the fluid-present runs at 10 kbar. The diagram is contoured with calculated isotherms at 10 kbar for the Fe–Mg exchange between both phases using average grossular and spessartine contents in garnet rims formed at 10 kbar. (c) Calculated temperatures for Fe–Mg exchange between garnet (with maximum Mg# and measured Ca and Mn) and staurolite vs run temperatures. (d) Calculated temperature vs measured garnet composition of fluid-present runs at 10 kbar compared with calculated garnet composition to make the calculated and run temperatures concordant [X_{grs} and X_{sps} averaged as in (b)]. The diagram is contoured with calculated isopleths of $Mg\#^{St}$. All calculations performed using model 5 of Koch-Müller (1997) for FMASH staurolite and the Fe–Mg solution model for garnet of Hackler & Wood (1989) with corrections for Ca and Mn after Lee & Ganguly (1988).

The behaviour of $Fe–Mg^{St–Grt}$ partitioning with temperature is illustrated in Fig. 9b, contoured with isotherms calculated at 10 kbar using the thermodynamic model 5 of Koch-Müller (1997) for FMASH staurolite and the Fe–Mg solution model of Hackler & Wood (1989) for garnet with corrections for Ca and Mn after Lee & Ganguly (1988), as indicated by Koch-Müller (1997). Our data plot within the field of normal partitioning, but approaching the locus of the azeotrope ($Mg\#^{Grt} = Mg\#^{St}$) as the run temperature rises,

as expected from the model. The temperatures calculated agree to a reasonable extent with run temperatures (Fig. 9c), although some of the calculated temperatures are lower. These discrepancies may be due to (1) the unaccounted energetic effects of Zn and Mn in the FMASH thermodynamic model of staurolite solid solution, (2) the unaccounted effect of Fe^{3+} in staurolite [set to zero in the calculations because, following Koch-Müller (1997, p. 187), Fe^{3+} is likely to be close to 3% of the total Fe content in this graphite-bearing system; see Holdaway *et al.* (1991, 1995)]; (3) the precise analysis of the rims of zoned garnets that may have higher Mg# than measured (Fig. 9d; see Carrington & Harley, 1995, p. 280); (4) imperfect equilibrium.

In general, the extent of partitioning between garnet and biotite decreases with rising temperature, in agreement with the well-known behaviour of $Fe–Mg^{Bt–Grt}$ partitioning (e.g. Ferry & Spear, 1978). For example, $\ln K_D^{Bt–Grt}[K_D^{Bt–Grt} = (Mg/Fe)^{Bt}/(Mg/Fe)^{Grt}]$ is equal to 1·528, 1·419 and 1·303, at 700, 725 and 750°C, respectively, and 10 kbar. However, there exist some inconsistencies (e.g. $\ln K_D^{Bt–Grt} = 1·339$ at 775°C, 10 kbar, higher than at 750°C, 10 kbar), which may be ascribed to problems with the precise analysis of garnet rims and/or the fine-grained laths of newly formed biotite. These problems are also indicated by the calculated garnet–biotite temperatures, which are several tens of degrees lower than nominal run temperatures [using, for example, the calibrations of Berman (1990) and Holdaway (2001)].

Melt–solids partitioning

The comparison of our results with other experimental studies that obtained supersolidus staurolite is not possible: Castro *et al.* (1999) did not report the composition of this phase, Vielzeuf & Montel (1994) did not obtain garnet coexisting with staurolite and did not report the analysis of the coexisting liquid, and Patiño Douce & Harris (1998) did not report analyses of coexisting garnet. However, the reported results of the last workers indicate $Mg\#^{St} < Mg\#^{L} < Mg\#^{Bt}$, consistent with our sequence $Mg\#^{Grt} < Mg\#^{St} < Mg\#^{L} < Mg\#^{Bt}$ at 725–775°C.

In their theoretical study, Spear *et al.* (1999) did not mention the type of partitioning used for their St-bearing supersolidus field. Within the St-absent supersolidus region, those workers followed the experimental results of Carrington & Harley (1995) for an invariant point involving Grt–Bt–Opx–Sil–Crd–Qtz–L at ~900°C, 8·8 kbar, where $Mg\#^{L} < Mg\#^{Grt} < Mg\#^{opx} < Mg\#^{Bt} < Mg\#^{Crd}$, and used $Mg\#^{Grt} < Mg\#^{St} < Mg\#^{Bt}$ within the St-bearing subsolidus region. As Spear *et al.* (1999) did not mention any reversal within the $P–T$ field modelled, we infer that they used $Mg\#^{L} < Mg\#^{Grt} < Mg\#^{St} < Mg\#^{Bt}$ in the St + L-bearing field. This type of partitioning, consistent with $Mg\#^{L} < Mg\#^{Grt} < Mg\#^{Bt}$ favoured by Abbott & Clarke (1979), Thompson (1982) and Abbott (1985), does not agree with our experimental sequences $Mg\#^{Grt} < Mg\#^{L} < Mg\#^{St} < Mg\#^{Bt}$ at 700°C and $Mg\#^{Grt} < Mg\#^{St} < Mg\#^{L} < Mg\#^{Bt}$ at 725–775°C, which, instead, are consistent with $Mg\#^{Grt} < Mg\#^{L} < Mg\#^{Bt}$ favoured by Green (1976), Clemens & Wall (1981), Grant (1985), Le Breton & Thompson (1988), Vielzeuf & Holloway (1988) and Patiño Douce (1996).

In summary, the run products compare well with other experimental results and natural data, and agree with equilibrium theory in that the composition of the phases and associated K_D values change systematically with varying pressure, temperature and water content. In consequence, we conclude that there exists an equilibrium field of supersolidus staurolite above the fluid-saturated solidus of the investigated sample. The consequences for petrogenetic grids appropriate for initial melting of metapelites are discussed below.

AN EXPERIMENTALLY CONSTRAINED KNFMASH GRID

Since Grant (1973) indicated that the stability of St + Ms + Qtz-bearing assemblages does not reach melt-present conditions and, consequently, refused to analyse the appropriate phase relations in his $P–T$ grid, this task has been routinely abandoned in the literature. To our knowledge, only Spear *et al.* (1999) have outlined the basic relationships in the KNFMASH system, although those workers admitted that their invariant-point relations were not fully worked out. The fluid-present solidus reaction proposed by Spear *et al.* (1999; see Fig. 2) is

$$Qtz + Ms + Bt + V = St + Grt + Als + L. \quad (2)$$

This reaction does not conform with our experiments in that it predicts the production of Al-silicate (and garnet). Moreover, this reaction is plagioclase-absent, and this seems unreasonable for a hydrous solidus reaction in the KNFMASH system under consideration [note that if albite were a reactant in reaction (2), one of the other phases must not be involved in the reaction; otherwise it would not correspond to a univariant reaction but to an invariant point]. For these reasons, we have developed a new KNFMASH grid using the partition constraints in the assemblages of our fluid-present experiments. The grid is appropriate for initial melting of metapelites, a region that has been by far less well investigated than higher-temperature regions appropriate for granulitic conditions.

KASH and KFASH topologies

The subsolidus, solidus and supersolidus phase relations among quartz, Al-silicate, muscovite, K-feldspar, biotite, garnet, staurolite, silicate melt and H_2O-fluid in the KASH and KFASH systems are shown in Fig. 10. For both systems, the subsolidus relationships were calculated using the program *Gibbs* (Spear & Menard, 1989) and the associated most recent thermodynamic data (F. S. Spear & J. T. Cheney, unpublished data, 2000). The KASH solidus and supersolidus relationships were taken from Thompson & Algor (1977), and agree with the KASH relations calculated by Spear *et al.* (1999) and Holland & Powell (2001). The solidus and supersolidus relations in the KFASH system, which involve the stability of invariant points [St,Als] and [St,Bt] (absent phases within brackets), have been constrained by the calculated subsolidus relations, Schreinemakers' rules, the slopes of the KASH solidus and supersolidus univariant reactions, and the relation $FeO/(FeO + K_2O + Al_2O_3)^{Ms} < FeO/(FeO + K_2O + Al_2O_3)^{L}$ (molar ratio) indicated by the experiments (Fig. 1d).

KNFASH topology

The consideration of component Na_2O and phase albite brings about a shift to lower temperature of the solidus reactions relative to the KFASH system. This effect causes the subsolidus degenerate reaction [Kfs,L,Bt,Ms] to intersect the peritectic melting reaction [Kfs,St,Bt] and invariant point [Kfs,Bt] emerges, making supersolidus staurolite stable (Fig. 11). In this figure, the location and slopes of the reactions are schematic, but constrained by the position and slopes of the subsolidus reaction [Kfs,L,Bt,Ms] and the initial melting reactions as developed by Thompson & Algor (1977), in addition to the relation $X_{Na}{}^{Ms} < X_{Na}{}^{Kfs} < X_{Na}{}^{L} < X_{Na}{}^{Pl}$[$X_{Na} = Na_2O/(Na_2O + K_2O)$, molar ratio] indicated by the experiments (Fig. 1b). It should be noted that invariant point [Kfs,Bt] projects twice in P–T space because the sign of the Clapeyron slope of the L-absent degenerate reaction [Kfs,L,Bt,Ms] changes sharply from positive within the sillimanite stability field to negative within the kyanite field and, hence, the P–T field of coexistence of St + L + Qtz + Ms + Pl + V takes the form of a pseudo-triangular window limited by the reactions (absent phases in place of the equal sign):

$$Ms + Grt + Qtz + Pl + V\,[Kfs,Bt,Als]\,St + L \quad (3)$$

$$Ms + St + Qtz + Pl\,[Kfs,Bt,V]\,Grt + Als + L. \quad (4)$$

KNFMASH topology

For the NKFMASH system (Fig. 12), the position and slopes of the supersolidus reactions are schematic, but constrained by the calculated subsolidus reaction [Kfs,L], the developed relations for the KNFASH system, and $Mg\#^{Grt} < Mg\#^{St} < Mg\#^{L} < Mg\#^{Bt} < Mg\#^{Ms}$ indicated by the experiments (Figs 1e and 9a). As in the KNFASH system, stable supersolidus staurolite is associated with invariant point [Kfs], which projects twice in P–T space, causing the shape of the St + L + Qtz + Ms + Pl + V field to take the form of a pseudo-triangular window. The fluid-present lower limit and fluid-absent upper limit of this field are

$$Pl + Ms + Qtz + Bt + Grt + V\,[Kfs,Als]\,St + L \quad (5)$$

$$Pl + Ms + Qtz + St\,[Kfs,V]\,Grt + Bt + Als + L \quad (6)$$

respectively. Reaction (5) [Kfs,Als] represents the fluid-present peritectic solidus of K-feldspar-absent relatively aluminous Fe-rich metapelites (i.e. that project above the Ms–Grt tie-line in the AKF diagram, and above the Grt–Bt tie-line in the AFM diagram, Figs 11 and 12) at intermediate pressure (i.e. in the range 6–10 kbar), and produces staurolite as a peritectic phase. At pressures below and above the twin projection of invariant point [Kfs], the peritectic solidus changes to reaction [Kfs,St] (Fig. 12), which produces Al-silicate rather than staurolite.

For different partition assumptions from those adopted above a similar St + L + Qtz + Ms + Pl + V field would be predicted, but the stoichiometry and arrangement of reactions around invariant point [Kfs] would be different. In particular, it is worth inspecting the possibility of Grt + St + L formation because of the textural ambiguity concerning the net consumption or production of garnet in the fluid-present runs. Garnet could be in the product of reaction (5):

$$Pl + Ms + Qtz + Bt + V\,[Kfs, Als]\,St + Grt + L \quad (5')$$

if $Mg\#^{Grt} < Mg\#^{St} < Mg\#^{Bt} < Mg\#^{L}$ (instead of $Mg\#^{Grt} < Mg\#^{St} < Mg\#^{L} < Mg\#^{Bt}$). Although this type of partitioning is not consistent with our experimental results and with the experimental results and/or inferences of other workers mentioned in the section on melt–solids partitioning, it has some foundation because Patiño Douce (1996) has indicated that the Fe–Mg partitioning between biotite and melt experiences a reversal at ~750°C and 10 kbar, causing

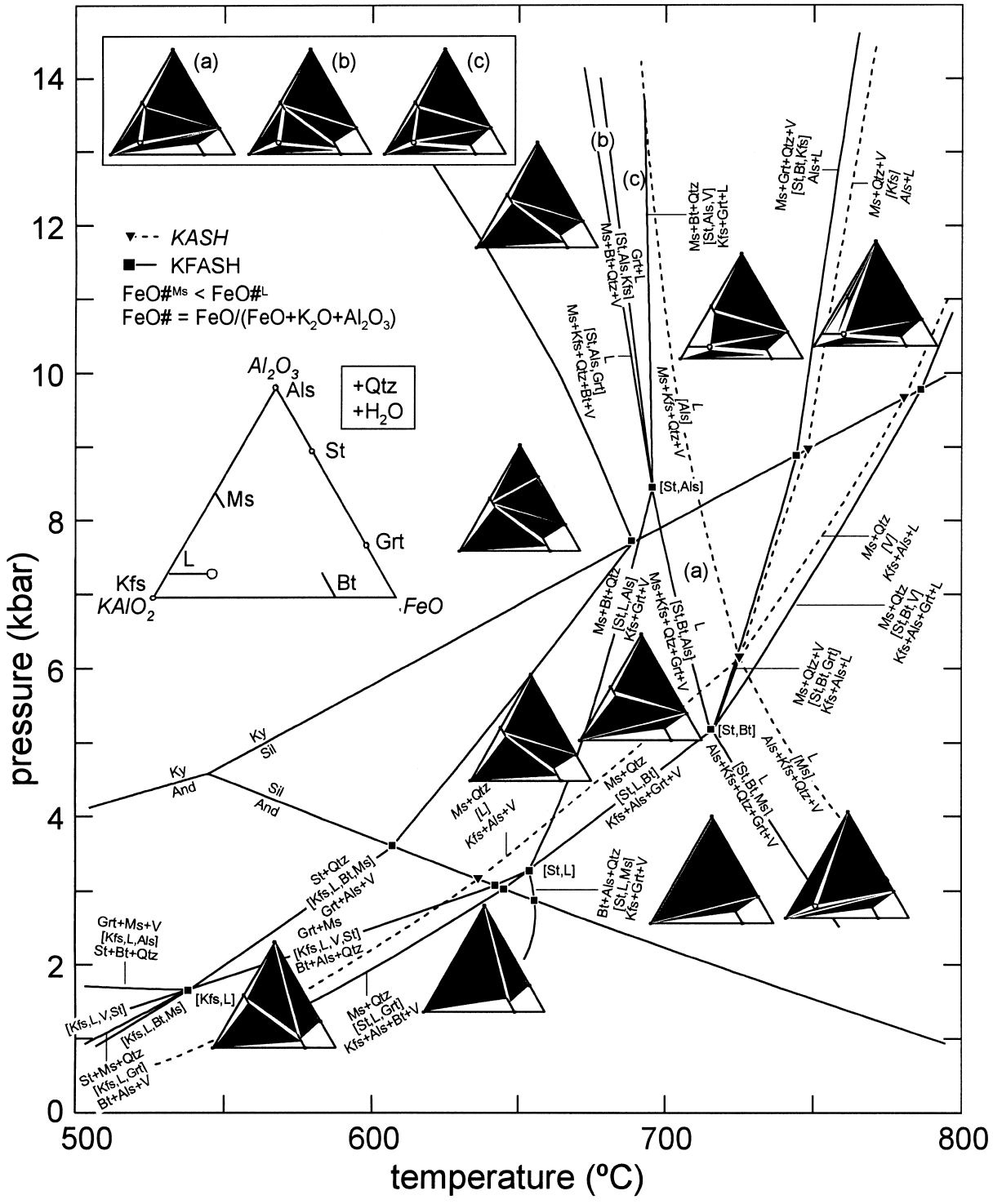

Fig. 10. Sub- and supersolidus phase relationships in the KASH and KFASH systems. (See text for details.)

$Mg\#^{Bt} < Mg\#^{L}$ at lower temperature and/or higher pressure [see García-Casco *et al.* (2001) for further development of this aspect]. That is, although our experiments indicate that garnet is consumed at the fluid-present St + L-forming solidus, its production is possible if Mg# in the melt is higher than in biotite. Additional experimental work is needed to clarify this point.

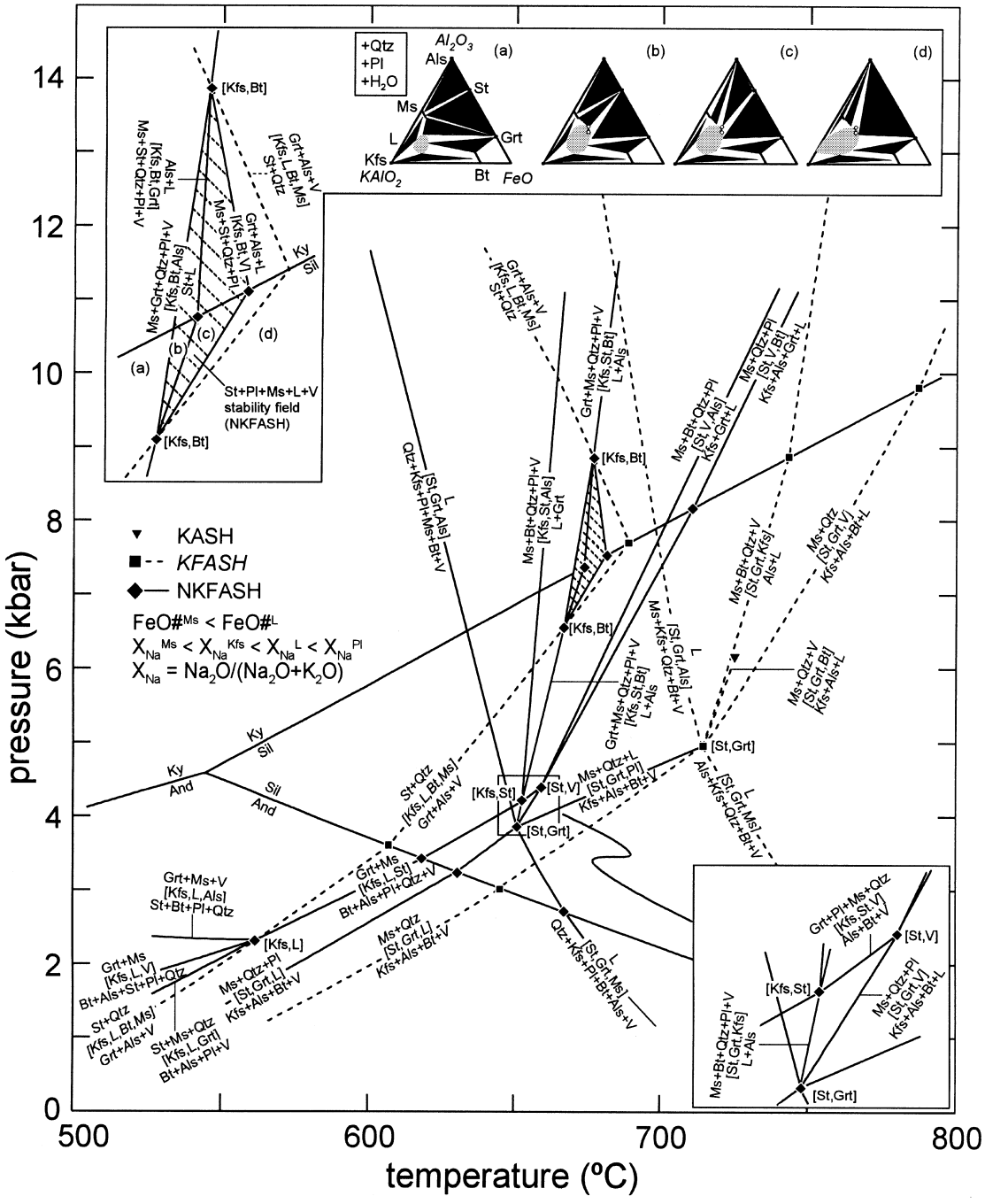

Fig. 11. NKFASH phase relationships. It should be noted that the relations around the twin projection of invariant point [Kfs,Bt] allow for the stability of St + L + Qtz + Ms + Pl + V-bearing assemblages (ruled pseudo-triangular area enlarged in the upper inset; the two small white circles in the associated AKF diagrams correspond to the compositions of experimental fluid-present melts at 750 and 775°C at 10 kbar; compare Fig. 1d). (See text for details.)

Comparison of the grid with experiments

The generalized melting reaction (1) compares well with the predicted fluid-present NKFMASH solidus reaction (5) [Kfs,Als], except for the presence of reactant Al-silicate in the former. Within the NKFMASH system, this cannot be explained in terms of overstepping of other reactions above the solidus, as they involve production of this phase (Fig. 12). A possible explanation is suggested by the corona-like textures involving formation of staurolite mantles

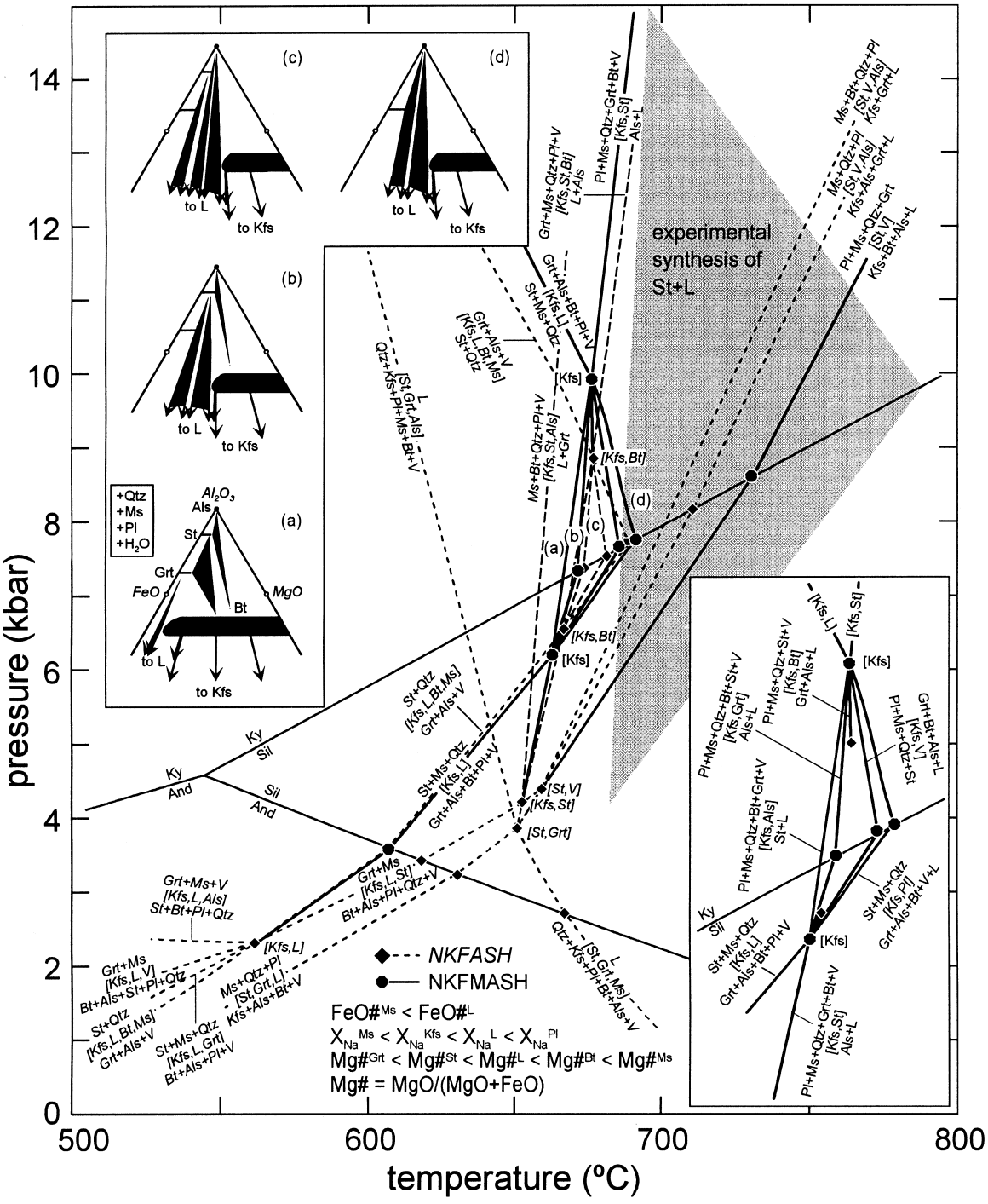

Fig. 12. NKFMASH phase relationships. The relations around the twin projection of invariant point [Kfs] that allow for the stability of St + L + Qtz + Ms + Pl + V-bearing assemblages are enlarged in the insets. (See text for details.) Also plotted is the experimental field of supersolidus staurolite (shaded region).

around kyanite relicts, which may indicate the instability of kyanite at the solidus and its metastable persistence at the run conditions, hence making possible a metastable growth of staurolite.

The experimental P–T field of supersolidus staurolite extends beyond the predicted stability limits of St + L + Qtz + Ms + Pl + V in the KNFMASH system (Fig. 12). The synthesis of staurolite by Patiño Douce

& Harris (1998) in a melting run of a medium-grade schist at 775°C, 10 kbar with 4 wt % added H_2O strengthens this discrepancy. The effects of extra components are difficult to assess because the predictable increase in the stability field of staurolite plus melt as a result of the incorporation of Zn (and/or Li; Dutrow *et al.*, 1986) in staurolite or B in the melt should be counterbalanced by the effect of Ca, Ti, Mn and C, which preferentially partition into plagioclase, biotite, garnet and fluid (as CO_2 and CH_4 species), respectively, causing the St + L + Qtz + Ms + Pl + V window to shrink. The effect of non-ideal behaviour of the solutions (particularly of staurolite) may also allow for a 25–50°C increase in the stability of the field of staurolite plus melt. But the most plausible explanation for this discrepancy is that the stability of supersolidus staurolite extends beyond the window in the absence of the whole assemblage that characterizes the window (i.e. St + L + Qtz + Ms + Pl + V). Plagioclase and muscovite are absent at ≥700°C and ≥725°C, respectively, and it could be argued that quartz, barely present as very small grains localized within the melt pools or within Al-silicate at ≥750°C, is effectively absent (within domains) at these conditions. Perhaps, also, Al-silicate (and quartz?) persisted metastably in these high-temperature runs. But even if part of the experimental P–T field of supersolidus staurolite is metastable, its identification is a strong argument for the existence of a stable field, as predicted in the KNFMASH grid.

The formation of staurolite in the fluid-absent experiments, on the other hand, coexisting with K-feldspar and at high temperature (825°C) is not predicted in the KNFMASH system (Fig. 12). These assemblages and conditions are possible only if staurolite is stabilized as a result of the effect of Zn (and/or Li). However, Zn contents are not particularly high (Table 8). This, and the fact that staurolite did not grow systematically within a distinct P–T range in the fluid-absent runs, suggests that its formation under fluid-absent conditions represents a non-equilibrium process. This is in agreement with the results of fluid-absent experiments by Vielzeuf & Montel (1994) and Montel & Vielzeuf (1997), who reported staurolite only in one run at 803°C, 10 kbar, and by Castro *et al.* (1999), who reported it at 800°C, 15 kbar (sample IT-521), and 900°C, 15 kbar (sample A7972). Those workers did not interpret these occurrences, but they may represent non-equilibrium because they are found irregularly within the wide P–T ranges investigated, and were not found in experiments by Vielzeuf & Montel (1994) and Montel & Vielzeuf (1997) using a metagreywacke glass rather than the natural sample. However, further experimental work is needed to confirm this conclusion in light of the results of Patiño Douce & Harris (1998), who suggested the stability of supersolidus staurolite in Qtz-bearing assemblages formed in fluid-absent melting and crystallization experiments of a medium-grade schist at 725–820°C, 6–10 kbar.

DISCUSSION AND CONCLUDING REMARKS

Scarcity of high-grade staurolite in nature

As indicated in the Introduction, the scarce natural examples of staurolite apparently stable in high-grade rocks seem to have formed because of the lack of quartz and/or the effect of Zn in stabilizing staurolite (e.g. Hollister, 1969; Ashworth, 1975; Goodman, 1993). Our experimental results and theoretical considerations suggest that these effects must be taken in combination with the availability of fluid in the stabilization of staurolite upon melting of metapelites.

In light of our results, potential candidates in which supersolidus St-bearing assemblages can be encountered are pelitic migmatites that lack K-feldspar and formed under fluid-present conditions. One example is the Isle of Pines migmatites, but staurolite is not present in these rocks conceivably because the prograde history at 11–12 kbar (García-Casco *et al.*, 2001) evaded the intersection of the St + L + Qtz + Ms + Pl + V window. This explanation can also apply to the Skagit gneiss, a classical example of fluid-present trondhjemitic migmatites that were metamorphosed to 9–10 kbar (Whitney, 1992) and where staurolite has been identified as subsolidus relicts within garnet (Misch, 1968; Yardley, 1978; Whitney & Irving, 1994). Lower-pressure fluid-present migmatites, however, also lack staurolite (e.g. Yardley & Barber, 1991), arguing for additional factors that shrink the stability of supersolidus staurolite.

Of these constraints, the bulk composition is important. Predictably, the bulk Mg# must be low, probably <0·4, and the aluminous character must be moderate to strong (i.e. bulk compositions that project above the Ms–Grt tie-line in the AKF diagram, and above the Grt–Bt tie-line in the AFM diagram). For bulk compositions with relatively high Mg# (probably ≥0·4), the prograde reaction paths at intermediate pressure would not encounter fluid-present melting reactions that stabilize staurolite and the melt-present assemblages should contain Bt + Als (± Crd ± Grt). An important additional constraint is the composition of the fluid. Dilution of H_2O in the fluid should shrink the stability of supersolidus staurolite to a considerable extent. This effect is expected because reaction (5) [Kfs,Als] and other fluid-present melting reactions that have H_2O in the reactant assemblage are

displaced to higher temperature as $X_{H_2O}^{fluid}$ decreases, whereas the subsolidus reaction

$$St + Ms + Qtz\ [Kfs,L]\ Grt + Als + Bt + Pl + V \quad (7)$$

(NKFMASH system, Fig. 12) is displaced to lower temperature. Because of these displacements, the P–T projections of invariant point [Kfs] approach one another along the fluid-absent reaction (6) [Kfs,V], causing the St + L + Qtz + Ms + Pl + V window to shrink and to completely disappear when they meet. The calculated displacement of the subsolidus reaction (7) [Kfs,L] for varying $X_{H_2O}^{fluid}$ in H_2O–CO_2 fluid mixtures suggests that St + L + Qtz + Ms + Pl + V-bearing assemblages should not form in fluid-present systems with $X_{H_2O}^{fluid} \leq 0{\cdot}7$. As the same applies to fluid-absent systems, the lack of staurolite in intermediate-pressure, aluminous, Fe-rich migmatites can be taken as an indication that partial melting processes in natural rocks take place under either reduced $X_{H_2O}^{fluid}$ or fluid-absent conditions.

However, even if a given pelitic terrane accomplishes the tight requirements of availability of fluid, fluid composition, bulk composition, chemical complexities of other phases, and P–T conditions for the intersection of the St + L + Qtz + Ms + Pl + V window, there is little chance for identifying staurolite formed at the fluid-present solidus because it would have been rapidly consumed upon prograde metamorphism—see reaction (6) [Kfs,V]—which typically evolves towards low-$X_{H_2O}^{fluid}$ or fluid-absent conditions once the H_2O in the fluid is incorporated into the melt. This is certainly expected in migmatitic terranes not affected by fluid infiltration because the insignificant porosity of rocks during metamorphism precludes the existence of significant amounts of fluid, but it also applies to migmatitic terranes affected by fluid infiltration because $X_{H_2O}^{fluid}$ may be set to low values upon melting. Only metastable relicts of supersolidus staurolite could be identified in typical pelitic migmatites formed well within the supersolidus region, and these may appear texturally and compositionally similar to medium-grade subsolidus staurolite included within porphyroblasts such as those present in the Skagit gneiss.

Fluid-absent melting of medium-grade metapelites

The phase relations involving staurolite at supersolidus conditions have been routinely ignored in studies of partial melting of metapelites, perhaps because of the scarcity of high-grade staurolite in nature and the widely accepted view that staurolite should react out during prograde metamorphism at subsolidus conditions in metapelites of normal composition. However, the existence of a stable field of St + L + Qtz + Ms + Pl + V-bearing assemblages makes necessary the existence of a fluid-absent St-breakdown reaction that produces melt—see reaction (6) [Kfs,V], Fig. 12. Thus, our results strengthen the suggestion of Thompson & Connolly (1995) and Spear *et al.* (1999) that fluid-absent melting of St + Ms + Qtz-bearing metapelites occurs. We are not aware of descriptions of this type of fluid-absent melting processes in nature, but the indication of Treloar (1985, p. 82) that 'staurolite breakdown was synchronous with partial melting' in the Dalradian of Connemara gives foundation for this type of melting reaction, which may have been overlooked in other occurrences. Upon prograde metamorphism at appropriate intermediate pressure, this type of melting reaction should be encountered at lower temperature than the fluid-absent melting of Ms + Qtz + Pl ([St,V] in Fig. 12), and should be taken into account in studies of fluid-absent migmatites even if the St-consuming reactions produce a small quantity of melt so as to make it difficult to detect in natural rocks (see Spear *et al.*, 1999).

Fluid-present melting of medium-grade metapelites

Potential conditions for the occurrence of staurolite in migmatites are aluminous Fe-rich bulk compositions, low temperature, intermediate pressure, presence of fluid, and high X_{H_2O} in the fluid (675–700°C, 6–10 kbar for $X_{H_2O} = 1$ in the KNFMASH system). Supersolidus staurolite formed in this type of low-temperature migmatite should be rapidly consumed during subsequent progressive fluid-absent melting. Thus, it appears that supersolidus St-bearing assemblages should be looked for in low-temperature, near-solidus, pelitic migmatites (formed near the kyanite–sillimanite boundary), and not in migmatitic areas formed well within the supersolidus region. These low-temperature pelitic migmatites should lack K-feldspar and contain muscovite and staurolite, and may resemble normal subsolidus schists except, at best, for the presence of discrete trondhjemitic segregations formed after crystallization of small amounts of melt so as to often be thought of as not having undergone melting. Perhaps the scarcity of supersolidus staurolite in nature is the result of the misinterpretation of low-temperature near-solidus St-bearing migmatites as medium-grade subsolidus schists. However, if properly identified, they must represent the lowest-temperature partially melted metapelites in nature.

ACKNOWLEDGEMENTS

We acknowledge Mike Holdaway, Alberto Patiño Douce and an anonymous reviewer, and editor Kurt Bucher, for perceptive comments and suggestions. Any mistake or obscurity is our own. This paper has received financial support from the Spanish DGES-MEC (Projects PB96-1426 and BTE2002-01011).

REFERENCES

Abbott, R. N., Jr (1985). Muscovite-bearing granites in the AFM liquidus projection. *Canadian Mineralogist* **23**, 553–561.

Abbott, R. N., Jr & Clarke, D. B. (1979). Hypothetical liquidus relationships in the subsystem Al_2O_3–FeO–MgO projected from quartz, alkali feldspar and plagioclase for $a(H_2O) < 1$. *Canadian Mineralogist* **17**, 549–560.

Ashworth, J. R. (1975). Staurolite at anomalously high grade. *Contributions to Mineralogy and Petrology* **53**, 281–291.

Ballevre, M., Pinardon, J., Kienast, J. & Vuichard, J. (1989). Reversal of Fe–Mg partitioning between garnet and staurolite in eclogite-facies metapelites from the Champtoceaux Nappe (Brittany, France). *Journal of Petrology* **30**, 1321–1349.

Barker, F. (1979). Trondhjemites: definition, environment and hypotheses of origin. In: Barker, F. (ed.) *Trondhjemites, Dacites and Related Rocks*. Amsterdam: Elsevier, pp. 1–12.

Berman, R. G. (1990). Mixing properties of Ca–Mg–Fe–Mn garnets. *American Mineralogist* **75**, 328–344.

Burnham, C. W. (1994). Development of the Burnham model for prediction of H_2O solubility in magmas. In: Carroll, M. R. & Holloway, J. R. (eds) *Volatiles in Magmas. Mineralogical Society of America, Reviews in Mineralogy* **30**, 123–129.

Carrington, D. P. & Harley, S. L. (1995). Partial melting and phase relations in high-grade metapelites: an experimental petrogenetic grid in the KFMASH system. *Contributions to Mineralogy and Petrology* **120**, 270–291.

Castro, A., Patiño Douce, A. E., Corretgé, G. L., De la Rosa, J., El Biad, M. & El Hmidi, H. (1999). Origin of peraluminous granites and granodiorites, Iberian Massif, Spain: an experimental test of granite petrogenesis. *Contributions to Mineralogy and Petrology* **135**, 255–276.

Castro, A., Corretgé, G. L., El Biad, M., El Hmidi, M., Fernandez, C. & Patiño Douce, A. E. (2000). Experimental constraints on Hercynian anatexis in the Iberian Massif, Spain. *Journal of Petrology* **10**, 1471–1488.

Chopin, Ch., Henry, C. & Michard, A. (1991). Geology and petrology of the coesite-bearing terrain, Dora Maira massif, western Alps. *European Journal of Mineralogy* **3**, 263–291.

Clemens, J. D. & Wall, V. J. (1981). Origin and crystallization of some peraluminous (S-type) granitic magmas. *Canadian Mineralogist* **19**, 111–131.

Connolly, J. A. D. & Cesare, B. (1993). C–O–H–S fluid composition and oxygen fugacity in graphitic metapelites. *Journal of Metamorphic Geology* **11**, 379–388.

Conrad, W. K., Nicholls, I. A. & Wall, V. J. (1988). Water-saturated and -undersaturated melting of metaluminous and peraluminous crustal compositions at 10 kb: evidence for the origin of silicic magmas in the Taupo Volcanic Zone, New Zealand, and other occurrences. *Journal of Petrology* **29**, 765–803.

Dirks, P. H. G. M., Hand, M. & Powell, R. (1991). The *P–T–* deformation path for a mid-Proterozoic, low-pressure terrane: the Reynolds Range, central Australia. *Journal of Metamorphic Geology* **9**, 641–661.

Dutrow, B. L. & Holdaway, M. J. (1989). Experimental determination of the upper thermal stability of Fe-staurolite + quartz at medium pressures. *Journal of Petrology* **30**, 229–248.

Dutrow, B. L., Holdaway, M. J. & Hinton, R. W. (1986). Lithium in staurolite and its petrologic significance. *Contributions to Mineralogy and Petrology* **94**, 469–506.

Ferry, J. M. & Spear, F. S. (1978). Experimental calibration of the partitioning of Fe and Mg between biotite and garnet. *Contributions to Mineralogy and Petrology* **66**, 113–117.

Fisher, G. W. (1989). Matrix analysis of metamorphic mineral assemblages and reactions. *Contributions to Mineralogy and Petrology* **102**, 69–77.

French, B. M. (1966). Some geological applications of equilibrium between graphite and a C–O–H gas phase at high temperatures and pressures. *Reviews of Geophysics* **4**, 233–251.

Fuhrman, M. L. & Lindsley, D. H. (1988). Ternary-feldspar modeling and thermometry. *American Mineralogist* **73**, 201–215.

Ganguly, J. (1972). Staurolite stability and related parageneses: theory, experiments and applications. *Journal of Petrology* **13**, 335–365.

Ganguly, J. & Saxena, S. K. (1987). *Mixtures and Mineral Reactions. Mineral and Rocks 19*. New York: Springer, 291 pp.

García-Casco, A. & Torres-Roldán, R. L. (1996). Disequilibrium induced by fast decompression in St–Bt–Grt–Ky–Sil–And metapelites from the Betic Belt (Southern Spain). *Journal of Petrology* **37**, 1207–1239.

García-Casco, A., Torres-Roldán, R. L., Millán, G., Monié, P. & Haissen, F. (2001). High-grade metamorphism and hydrous melting of metapelites in the Pinos terrane (W Cuba): evidence for crustal thickening and extension in the northern Caribbean collisional belt. *Journal of Metamorphic Geology* **19**, 699–715.

Goodman, S. (1993). Survival of zincian staurolite to upper amphibolite facies metamorphic grade. *Mineralogical Magazine* **57**, 736–739.

Graessner, T. & Schenk, V. (2001). An exposed Hercynian deep crustal section in the Sila massif of northern Calabria: mineral chemistry, petrology and a *P–T* path of granulite-facies metapelitic migmatites and metabasites. *Journal of Petrology* **42**, 931–961.

Grant, J. A. (1973). Phase equilibria in high grade metamorphism and partial melting of pelitic rocks. *American Journal of Science* **273**, 289–317.

Grant, J. A. (1985). Phase equilibria in partial melting of pelitic rocks. In: Ashworth, J. R. (ed.) *Migmatites*. Glasgow: Blackie, pp. 86–144.

Green, T. H. (1976). Experimental generation of cordierite- or garnet-bearing granitic liquids from a pelitic composition. *Geology* **4**, 85–88.

Green, T. H. (1977). Garnet in silicic liquids and its possible use as a *P–T* indicator. *Contributions to Mineralogy and Petrology* **65**, 59–67.

Gardien, V., Thompson, A. B., Grujic, D. & Ulmer, P. (1995). Experimental melting of biotite + plagioclase + quartz + or – muscovite assemblages and implications for crustal melting. *Journal of Geophysical Research, B, Solid Earth and Planets* **100**, 15581–15591.

Gromet, L. P., Dymek, R. F., Haskin, L. A. & Korotev, R. L. (1984). The 'North American shale composite': its compilation, major and trace element characteristics. *Geochimica et Cosmochimica Acta* **48**, 2469–2482.

Hackler, R. T. & Wood, B. J. (1989). Experimental determination of Fe and Mg exchange between garnet and olivine and

estimation of Fe–Mg mixing properties of garnet. *American Mineralogist* **74**, 994–999.

Hawthorne, F. C. (1995). Light lithophile elements in metamorphic rock-forming minerals. *European Journal of Mineralogy* **7**, 607–622.

Holdaway, M. J. (2001). Recalibration of the GASP barometer in light of recent garnet and plagioclase activity models and versions of the garnet–biotite geothermometer. *American Mineralogist* **86**, 1117–1129.

Holdaway, M. J., Mukhopadhyay, B., Dyar, M. D., Dutrow, B. L., Rumble, D., III & Grambling, J. A. (1991). A new perspective on staurolite crystal chemistry: use of stoichiometric and chemical end-members for a mole fraction model. *American Mineralogist* **76**, 1910–1919.

Holdaway, M. J., Mukhopadhyay, B. & Dutrow, B. L. (1995). Thermodynamic properties of stoichiometric staurolite $H_2Fe_4Al_{18}Si_8O_{48}$ and $H_6Fe_2Al_{18}Si_8O_{48}$. *American Mineralogist* **80**, 520–533.

Holland, T. J. B. & Powell, R. (2001). Calculation of phase relations involving haplogranitic melts using an internally consistent thermodynamic dataset. *Journal of Petrology* **42**, 676–683.

Hollister, L. S. (1969). Contact metamorphism in the Kwoiek area of British Columbia: an end member of the metamorphic process. *Geological Society of America Bulletin* **80**, 2465–2494.

Holtz, F., Behrens, H., Dingwell, D. B. & Johannes, W. (1995). H_2O solubility in haplogranitic melts: compositional, pressure and temperature dependence. *American Mineralogist* **80**, 94–108.

Holtz, F., Johannes, W., Tamic, N. & Behrens, H. (2001). Maximum and minimum water contents of granitic melts generated in the crust: a reevaluation and implications. *Lithos* **56**, 1–14.

Huang, W. L. & Wyllie, P. J. (1974). Melting relations of muscovite with quartz and sanidine in the K_2O–Al_2O_3–SiO_2–H_2O system to 30 kbars and an outline of paragonite melting reactions. *American Journal of Science* **274**, 378–395.

Jának, M., Hurai, V., Ludhová, L., O'Brien, P. J. & Horn, E. E. (1999). Dehydration melting and devolatilization during exhumation of high-grade metapelites: the Tatra Mountains, Western Carpathians. *Journal of Metamorphic Geology* **17**, 379–395.

Johannes, W. & Holtz, F. (1996). *Petrogenesis and Experimental Petrology of Granitic Rocks*. New York: Springer, 335 pp.

Jones, K. A. & Brown, M. (1990). High-temperature 'clockwise' P–T paths and melting in the development of regional migmatites: an example from southern Brittany, France. *Journal of Metamorphic Geology* **8**, 551–578.

Koch-Müller, M. (1997). Experimentally determined Fe–Mg exchange between synthetic staurolite and garnet in the system MgO–FeO–Al_2O_3–SiO_2–H_2O. *Lithos* **41**, 185–212.

Kretz, R. (1983). Symbols for rock-forming minerals. *American Mineralogist* **68**, 277–279.

Lambert, I. B., Roberston, J. K. & Wyllie, P. J. (1969). Melting reactions in the system $KAlSi_3O_8$–SiO_2–H_2O to 18·5 kbar. *American Journal of Science* **267**, 609–626.

Le Breton, N. & Thompson, A. B. (1988). Fluid-absent (dehydration) melting of biotite in metapelites in the early stages of crustal anatexis. *Contributions to Mineralogy and Petrology* **99**, 226–237.

Lee, H. Y. & Ganguly, J. (1988). Equilibrium composition of coexisting garnet and orthopyroxene: experimental determinations in the system FeO–MgO–Al_2O_3–SiO_2, and applications. *Journal of Petrology* **29**, 93–113.

Millán, G. (1981). Geología del macizo metamórfico de la Isla de la Juventud. *Ciencias de la Tierra y del Espacio* **3**, 3–22.

Millán, G. (1997*a*). Geología del macizo metamórfico de la Isla de la Juventud. In: Furrazola Bermúdez, G. F. & Núñez Cambra, K. E. (eds) *Estudios sobre Geología de Cuba*. Havana: Centro Nacional de Información Geológica, pp. 259–270.

Millán, G. (1997*b*). Posición estratigráfica de las metamorfitas cubanas. In: Furrazola Bermúdez, G. F. & Núñez Cambra, K. E. (eds) *Estudios sobre Geología de Cuba*. Havana: Centro Nacional de Información Geológica, pp. 251–258.

Misch, P. (1968). Plagioclase compositions and non-anatectic origin of migmatitic gneisses in Northern Cascades mountains of Washington State. *Contributions to Mineralogy and Petrology* **17**, 1–70.

Montel, J. M. & Vielzeuf, D. (1997). Partial melting of metagreywackes, Part II. Compositions of minerals and melts. *Contributions to Mineralogy and Petrology* **128**, 176–196.

Ohmoto, H. & Kerrick, D. (1977). Devolatilization equilibria in graphitic systems. *American Journal of Science* **277**, 1013–1044.

Paillat, O., Elphick, S. C. & Brown, W. L. (1992). The solubility of water in $NaAlSi_3O_8$ melts: a re-examination of Ab–H_2O phase relationships and critical behaviour at high pressures. *Contributions to Mineralogy and Petrology* **112**, 490–500.

Patiño Douce, A. E. (1993). Titanium substitution in biotite: an empirical model with applications to thermometry, O_2 and H_2O barometries, and consequences for biotite stability. *Chemical Geology* **108**, 133–162.

Patiño Douce, A. E. (1996). Effects of pressure and H_2O content on the composition of primary crustal melts. *Transactions of the Royal Society of Edinburgh, Earth Sciences* **87**, 11–21.

Patiño Douce, A. E. (1999). What do experiments tell us about the relative contributions of crust and mantle to the origin of granitic magmas? In: Castro, A., Fernández, C. & Vigneresse, J. L. (eds) *Understanding Granites: Integrating New and Classical Techniques. Geological Society, London, Special Publications* **168**, 55–75.

Patiño Douce, A. E. & Beard, J. S. (1994). H_2O loss from hydrous melts during fluid-absent piston cylinder experiments. *American Mineralogist* **79**, 585–588.

Patiño Douce, A. E. & Beard, J. S. (1995). Dehydration-melting of biotite gneiss and quartz amphibolite from 3 to 15 kbar. *Journal of Petrology* **36**, 707–738.

Patiño Douce, A. E. & Beard, J. S. (1996). Effects of P, $f(O_2)$ and Mg/Fe ratio on dehydration melting of model metagreywackes. *Journal of Petrology* **37**, 999–1024.

Patiño Douce, A. E. & Harris, N. (1998). Experimental constraints on Himalayan anatexis. *Journal of Petrology* **39**, 689–710.

Pattison, D. R. M. & Tracy, R. J. (1991). Phase equilibria and thermobarometry of metapelites. In: Kerrick, D. M. (ed.) *Contact Metamorphism. Mineralogical Society of America, Reviews in Mineralogy* **26**, 105–206.

Pickering, J. M. & Johnston, A. D. (1998). Fluid-absent melting behavior of a two-mica metapelite: experimental constraints on the origin of Black Hills granite. *Journal of Petrology* **39**, 1787–1804.

Rao, B. B. & Johannes, W. (1979). Further data on the stability of staurolite + quartz and related assemblages. *Neues Jahrbuch für Mineralogie, Monatshefte* **10**, 437–447.

Rasband, W. (1997). *NIH Image*. Washington, DC: National Institute of Health.

Rice, J. M. (1985). Experimental partitioning of Fe and Mg between coexisting staurolite and garnet. *EOS Transactions, American Geophysical Union* **66**, 1127.

Richardson, S. W. (1968). Staurolite stability in a part of the system: Fe–Al–Si–O–H. *Journal of Petrology* **9**, 467–488.

Saxena, S. K. (1973). *Thermodynamics of Rock-Forming Crystalline Solutions*. New York: Springer, 188 pp.

Somin, M. L. & Millán, G. (1981). *Geology of the Metamorphic Complexes of Cuba*. Moscow: Nauka, 219 pp. (in Russian).

Spear, F. S. & Cheney, J. T. (1989). A petrogenetic grid for pelitic schists in the system SiO_2–Al_2O_3–FeO–MgO–K_2O–H_2O. *Contributions to Mineralogy and Petrology* **101**, 149–164.

Spear, F. S. & Menard, T. (1989). Program GIBBS: a generalized Gibbs method algorithm. *American Mineralogist* **74**, 942–943.

Spear, F. S., Kohn, M. J. & Cheney, J. T. (1999). *P–T* paths from anatectic pelites. *Contributions to Mineralogy and Petrology* **134**, 17–32.

Storre, B. & Karotke, E. (1972). Experimental data on melting reactions of muscovite + quartz in the system K_2O–Al_2O_3–SiO_2–H_2O to 20 kbar water pressure. *Contributions to Mineralogy and Petrology* **36**, 343–345.

Thompson, A. B. (1982). Dehydration melting of pelitic rocks and the generation of H_2O-undersaturated granitic liquids. *American Journal of Science* **282**, 1567–1595.

Thompson, A. B. & Algor, J. R. (1977). Model system for anatexis of pelitic rocks. I. Theory of melting reactions in the system $KAlO_2$–$NaAlO_2$–Al_2O_3–SiO_2–H_2O. *Contributions to Mineralogy and Petrology* **63**, 247–269.

Thompson, A. B. & Connolly, J. A. D. (1995). Melting of the continental crust: some thermal and petrological constraints on anatexis in continental collision zones and other tectonic settings. *Journal of Geophysical Research* **100**, 15565–15579.

Torres-Roldán, R. L., García-Casco, A. & García-Sánchez, P. A. (2000). CSpace: an integrated workplace for the graphical and algebraic analysis of phase assemblages on 32-bit Wintel platforms. *Computers and Geosciences* **26**, 779–793.

Treloar, P. J. (1985). Metamorphic conditions in central Connemara, Ireland. *Journal of the Geological Society, London* **142**, 77–86.

Truckenbrodt, J. & Johannes, W. (1999). H_2O loss during piston-cylinder experiments. *American Mineralogist* **84**, 1333–1335.

Vielzeuf, D. & Holloway, J. R. (1988). Experimental determination of the fluid-absent melting relations in the pelitic system. Consequences for crustal differentiation. *Contributions to Mineralogy and Petrology* **98**, 257–276.

Vielzeuf, D. & Montel, J. M. (1994). Partial melting of metagreywackes. Part I. Fluid-absent experiments and phase relationships. *Contributions to Mineralogy and Petrology* **117**, 375–393.

Vielzeuf, D. & Schmidt, M. W. (2001). Melting relations in hydrous system revisited: application to metapelites, metagreywackes and metabasalts. *Contributions to Mineralogy and Petrology* **141**, 251–267.

White, R. W., Powell, R. & Holland, T. J. B. (2001). Calculation of partial melting equilibria in the system Na_2O–CaO–K_2O–FeO–MgO–Al_2O_3–SiO_2–H_2O (NCKFMASH). *Journal of Metamorphic Geology* **19**, 139–153.

Whitney, D. L. (1992). High-pressure metamorphism in the Western Cordillera of North America: an example from the Skagit Gneiss, North Cascades. *Journal of Metamorphic Geology* **10**, 71–85.

Whitney, D. L. & Irving, A. J. (1994). Origin of K-poor leucosomes in a metasedimentary migmatite complex by ultrametamorphism, synmetamorphic magmatism and subsolidus processes. *Lithos* **32**, 173–192.

Wilson, C. J. L. & Powell, L. (2001). Strain localisation and high-grade metamorphism at Broken Hill, Australia: a view from the Southern Cross area. *Tectonophysics* **335**, 193–210.

Yardley, B. W. D. (1976). Deformation and metamorphism of Dalradian rocks and the evolution of the Connemara cordillera. *Journal of the Geological Society, London* **132**, 521–542.

Yardley, B. W. D. (1978). Genesis of the Skagit Gneiss migmatites, Washington, and the distinction between possible mechanisms of migmatization. *Geological Society of America Bulletin* **89**, 941–951.

Yardley, B. W. D. (1981). A note on the composition and stability of Fe-staurolite. *Neues Jahrbuch für Mineralogie, Monatshefte* **3**, 127–132.

Yardley, B. W. D. & Barber, J. P. (1991). Melting reactions in the Connemara Schists: the role of fluid infiltration in the formation of amphibolite facies migmatites. *American Mineralogist* **76**, 848–856.